

The Distribution of Metallicities in the Local Galactic Interstellar Medium*

ADAM M. RITCHEY,¹ EDWARD B. JENKINS,² J. MICHAEL SHULL,³ BLAIR D. SAVAGE,⁴ S. R. FEDERMAN,⁵ AND DAVID L. LAMBERT⁶

¹*Eureka Scientific, 2452 Delmer Street, Suite 100, Oakland, CA 96402, USA*

²*Department of Astrophysical Sciences, Princeton University, Princeton, NJ 08544, USA*

³*Department of Astrophysical and Planetary Sciences and CASA, University of Colorado, Boulder, CO 80309, USA*

⁴*Department of Astronomy, University of Wisconsin-Madison, Madison, WI 53706, USA[†]*

⁵*Department of Physics and Astronomy, University of Toledo, Toledo, OH 43606, USA*

⁶*W. J. McDonald Observatory and Department of Astronomy, University of Texas at Austin, Austin, TX 78712, USA*

ABSTRACT

In this investigation, we present an analysis of the metallicity distribution that pertains to neutral gas in the local Galactic interstellar medium (ISM). We derive relative ISM metallicities for a sample of 84 sight lines probing diffuse atomic and molecular gas within 4 kpc of the Sun. Our analysis is based, in large part, on column density measurements reported in the literature for 22 different elements that are commonly studied in interstellar clouds. We supplement the literature data with new column density determinations for certain key elements and for several individual sight lines important to our analysis. Our methodology involves comparing the relative gas-phase abundances of many different elements for a given sight line to simultaneously determine the strength of dust depletion in that direction and the overall metallicity offset. We find that many sight lines probe multiple distinct gas regions with different depletion properties, which complicates the metallicity analysis. Nevertheless, our results provide clear evidence that the dispersion in the metallicities of neutral interstellar clouds in the solar neighborhood is small (~ 0.10 dex) and only slightly larger than the typical measurement uncertainties. We find no evidence for the existence of very low metallicity gas (as has recently been reported by De Cia et al.) along any of the 84 sight lines in our sample. Our results are consistent with a local Galactic ISM that is well mixed and chemically homogeneous.

Keywords: interstellar medium — interstellar abundances — diffuse interstellar clouds

1. INTRODUCTION

Most models of Galactic chemical evolution assume that the gas enriched in the products of stellar nucleosynthesis is instantaneously mixed into the interstellar medium (ISM; e.g., Timmes et al. 1995; Chiappini et al. 1997). The instantaneous mixing assumption, while not entirely realistic, can nevertheless yield model predic-

tions that succeed in reproducing the evolutionary abundance trends of the elements (e.g., François et al. 2004). There is strong observational evidence that supports the idea that the ISM, at a given Galactocentric distance, is well mixed and chemically homogeneous. In a comprehensive study of abundances in early B-type stars in the solar neighborhood, Nieva & Przybilla (2012) found very narrow distributions in the abundances of He, C, N, O, Ne, Mg, Si, and Fe, with standard deviations equal to 0.05 dex or less. Luck (2018) conducted a thorough examination of abundances in hundreds of classical Cepheid stars. For Cepheids located within 1 kpc of the Sun, Luck (2018) finds that the standard deviation in the values of $[\text{Fe}/\text{H}]$ is 0.10 dex.

Arellano-Córdova et al. (2021) presented results on radial abundance gradients in the Milky Way from a uniform analysis of 42 Galactic H II regions. They find

Corresponding author: Adam M. Ritchey
ritchey.astro@gmail.com

* Based in part on observations made with the NASA/ESA Hubble Space Telescope, obtained from the MAST data archive at the Space Telescope Science Institute. STScI is operated by the Association of Universities for Research in Astronomy, Inc., under NASA contract NAS5-26555. Based in part on data obtained from the ESO Science Archive Facility with DOI: <https://doi.org/10.18727/archive/50>.

[†] Deceased.

that the dispersion in the values of O/H and N/H with respect to the computed gradients is 0.07 and 0.11 dex, respectively. [Ritchey et al. \(2018\)](#) reported on the gas-phase abundances of O and several neutron-capture elements for a sample of 128 sight lines probing the neutral ISM in the solar vicinity. The analysis of elemental abundances in the neutral ISM is complicated by the presence of significant depletion onto dust grains for most elements (e.g., [Jenkins 2009](#)). Adopting the methodology of [Jenkins \(2009\)](#), [Ritchey et al. \(2018\)](#) identified and modelled the depletion behaviors for the elements they considered. For O, Ge, and Kr, which have the largest number of abundance measurements in the sample, [Ritchey et al. \(2018\)](#) find that the dispersions in the abundances with respect to the depletion trends are 0.07, 0.10, and 0.07 dex, respectively. Numerous other studies have examined the homogeneity of gas-phase interstellar abundances in the solar neighborhood (e.g., [Cardelli et al. 1996](#); [Meyer et al. 1997, 1998](#); [Cartledge et al. 2003, 2004, 2006](#)). These studies have generally found only small variations in the gas-phase abundances once the effects of dust-grain depletion are taken into account.

From a theoretical perspective, the Galactic ISM is expected to be well mixed in the azimuthal direction (e.g., [Edmunds 1975](#); [Roy & Kunth 1995](#)). Turbulent transport in the shear flow of differential rotation should reduce azimuthal inhomogeneities in large disk galaxies like the Milky Way within a characteristic timescale of 10^9 yr ([Roy & Kunth 1995](#)). On smaller scales, turbulent mixing due to supernova explosions ([de Avillez & Mac Low 2002](#)) and thermal instabilities ([Yang & Krumholz 2012](#)) leads to even shorter mixing timescales. [Petit et al. \(2015\)](#) studied turbulent mixing driven by gravitational instabilities and found that metallicity inhomogeneities are destroyed in the azimuthal direction in less than a galactic orbital period.

Recently, however, [De Cia et al. \(2021\)](#) reported finding large metallicity variations in the neutral ISM toward stars located within 3 kpc of the Sun. After applying two separate techniques to account for dust-grain depletion, [De Cia et al. \(2021\)](#) report depletion-corrected metallicities in the range $-0.76 \leq [M/H] \leq +0.26$ dex for their sample of 25 sight lines. They report a mean value of $[M/H]$ of -0.26 dex and a standard deviation of 0.28 dex. [De Cia et al. \(2021\)](#) attribute the low metallicity material to the effects of metal-poor infall from high-velocity clouds combined with inefficient mixing in the Galactic disk. However, these conclusions run counter to the growing body of evidence from observational and theoretical work that the ISM, at a given

Galactocentric distance, is (and is expected to be) well mixed and chemically homogeneous.

Upon closer examination, we find that there are serious flaws in the analysis techniques adopted in [De Cia et al. \(2021\)](#) that undermine their conclusions. For example, they derive column densities from relatively strong interstellar absorption lines (e.g., Zn II $\lambda\lambda 2026, 2062$) using spectra obtained at moderate resolution ($\Delta v \sim 10 \text{ km s}^{-1}$). While attempts are made to account for unresolved saturation in the absorption profiles, it appears that these attempts are inadequate in some cases and that many of the Zn II column densities in particular may be underestimated. A more serious issue is that the elements used by [De Cia et al. \(2021\)](#) for their metallicity estimates (Si, Ti, Cr, Fe, Ni, and Zn) are the more refractory elements, which are significantly impacted by dust depletion. Volatile elements (such as C, N, O, and Kr), which are more reliable metallicity indicators, are not included in their analysis, even though they yield conflicting results.

In this investigation, we seek to derive, in a much more definitive way, the metallicity distribution for the local Galactic ISM. Our analysis relies mainly on high-quality gas-phase abundance measurements reported in the literature. However, we also obtain new column density determinations for certain key elements and for several important and/or interesting sight lines in order to fill in some of the gaps in the literature data. The methodology used in our metallicity analysis, which is based on the unified representation of interstellar depletions devised by [Jenkins \(2009\)](#), is described in Section 2. The sources and methods used to obtain column density measurements for our sample are described in Section 3. The metallicity estimates themselves are provided in Section 4. In Section 5.1, we present a detailed comparison between our metallicity determinations and those of [De Cia et al. \(2021\)](#). In Section 5.2, we discuss the implications of our results in the context of other measurements of metallicity variations in the Galactic disk. We summarize our conclusions in Section 6. An appendix provides a compilation of all of the column density measurements used in the metallicity analysis.

2. METHODOLOGY

In a comprehensive analysis of interstellar depletions, [Jenkins \(2009\)](#) utilized measurements of elemental abundances reported in the literature for a sample of 243 sight lines to examine the depletion characteristics of 17 different elements. [Jenkins \(2009\)](#) developed a unified representation of gas-phase element depletions predicated on the empirical observation that, while different elements exhibit different degrees of depletion,

the depletions of most elements tend to increase in a systematic way as the overall strength of depletions increases from one line of sight to the next. Sight lines with stronger depletions are thought to contain higher proportions of denser and/or colder gas (Spitzer 1985; Savage & Sembach 1996), while sight lines with very low depletions may contain grains that have been partially destroyed through sputtering in interstellar shocks (e.g., Shull et al. 1977). The increase in the overall strength of depletions, from low-density diffuse atomic gas to higher-density diffuse molecular clouds, may then be regarded as evidence of grain growth in the ISM (Dwek & Scalo 1980; Jenkins et al. 1986; Savage & Sembach 1996; Jenkins 2009, 2013). Many grain history calculations have suggested that the survival of dust grains against destruction via shock sputtering requires continued growth in diffuse clouds (Seab & Shull 1983; Jones et al. 1994; Slavin et al. 2015). With these considerations, Jenkins (2009) defined a sight-line depletion strength factor, denoted F_* , which indicates the extent to which grain growth has progressed in the gas sampled by a particular line of sight. The value of F_* for any given sight line is based on a weighted average of the available observed depletions for that direction (see Equation (4) in Jenkins 2009). Sight lines showing strong depletions, such as those seen in the low velocity ($v_{\text{LSR}} = -1 \text{ km s}^{-1}$) component toward ζ Oph (e.g., Savage et al. 1992), have depletion strengths near $F_* = 1$, while those with the weakest depletions have F_* values close to zero.

The depletion of an element X from the gas phase is defined with respect to an adopted cosmic reference abundance, typically the solar system abundance of the element. In logarithmic terms, we have:

$$[X/H] = \log N(X) - \log N(\text{H}_{\text{tot}}) - \log(X/H)_{\odot}, \quad (1)$$

where $N(X)$ is the total column density of element X in its dominant ionization stage, $N(\text{H}_{\text{tot}}) = N(\text{H I}) + 2N(\text{H}_2)$ is the total hydrogen column density along the line of sight, and $(X/H)_{\odot}$ is the solar reference abundance. In the framework developed by Jenkins (2009), the logarithmic depletion of an element depends on the sight-line depletion strength factor according to:

$$[X/H] = B_X + A_X(F_* - z_X), \quad (2)$$

where the depletion parameters A_X , B_X , and z_X are unique to each specific element. As described in more detail in Jenkins (2009), the slope parameter A_X indicates how quickly the depletion of a particular element strengthens as the growth of dust grains progresses within interstellar clouds (see also Jenkins 2013). The

intercept parameter B_X indicates the expected depletion of element X at $F_* = z_X$, where z_X represents a weighted mean value of F_* for the particular set of sight lines with depletion measurements available for that element. Values of the coefficients A_X and B_X are obtained for a specific element through the evaluation of a least-squares linear fit, with $[X/H]$ as the dependent variable and F_* the independent variable. (The reason for the additional term involving z_X in Equation (2) is that, for a particular choice of z_X , there is a near zero covariance between the formal fitting errors for the solutions of A_X and B_X (see Jenkins 2009).)

Jenkins (2009) obtained values of the element-specific depletion parameters for 17 different elements: C, N, O, Mg, Si, P, S, Cl, Ti, Cr, Mn, Fe, Ni, Cu, Zn, Ge, and Kr. Later, Ritchey et al. (2018), adopting the Jenkins (2009) methodology, derived depletion parameters for B, Ga, As, Cd, Sn, and Pb and re-evaluated the depletion parameters for O, Ge, and Kr using larger samples of elemental abundance measurements. Most recently, Ritchey et al. (2023) re-determined the values of the depletion parameters for the elements P and Cl, both to account for recent updates in the oscillator strengths of the relevant P II and Cl I transitions and to correct for a deficiency in the Cl analysis presented in Jenkins (2009). In the original analysis, Jenkins (2009) considered only Cl II column densities in deriving total Cl abundances. However, Cl is unique among most other elements commonly studied in the ISM in that either its neutral or its singly-ionized form can dominate the total abundance depending on the amount of molecular hydrogen present along the line of sight (e.g., Jura & York 1978). Ritchey et al. (2023) included column densities of both Cl I and Cl II in their derivations of total Cl abundances and Cl depletion factors.

Based on the formalism developed to study gas-phase element depletions, Jenkins (2009) proposed a method that could be used to examine the metallicities of distant (extragalactic) absorption systems, such as those seen in the optical spectra of high-redshift quasars. As we show below, the metallicity determined according to this method is the metallicity of the absorption system relative to the average metallicity that characterizes the local Galactic ISM. (Hereafter, we refer to this quantity as the “relative ISM metallicity”.) In the present work, we use this method to examine the spread in the metallicities determined for sight lines probing the solar neighborhood (out to ~ 4 kpc).

To determine the relative ISM metallicity for a given sight line, we first equate the two expressions for $[X/H]$ presented in Equations (1) and (2):

$$\log N(X) - \log N(\text{H}_{\text{tot}}) - \log(X/\text{H})_{\odot} = B_X + A_X(F_* - z_X). \quad (3)$$

Rearranging terms, we have:

$$\log N(X) - \log(X/\text{H})_{\odot} - B_X + A_X z_X = \log N(\text{H}_{\text{tot}}) + F_* A_X. \quad (4)$$

The quantity $N(\text{H}_{\text{tot}})$ appearing on the righthand side of Equation (4) can be interpreted as the total hydrogen column density that would be expected based on the column density of element X and the overall strength of depletions along the line of sight (F_*). However, this expectation holds only if the metallicity of the gas is equal to the average ISM metallicity in the solar neighborhood. If the metallicity is somewhat different, then the true hydrogen column density will be higher or lower than the predicted value. Thus, if the total hydrogen column density is known independently from observations, we can rewrite Equation (4) in terms of the relative ISM metallicity:

$$[\text{M}/\text{H}]_{\text{ISM}} = \log N(\text{H}_{\text{tot}})_{\text{pred}} - \log N(\text{H}_{\text{tot}})_{\text{obs}}. \quad (5)$$

Subtracting $\log N(\text{H}_{\text{tot}})_{\text{obs}}$ from both sides of Equation (4) yields:

$$[\text{X}/\text{H}]_{\text{obs}} - B_X + A_X z_X = [\text{M}/\text{H}]_{\text{ISM}} + F_* A_X, \quad (6)$$

where

$$[\text{X}/\text{H}]_{\text{obs}} = \log N(X) - \log N(\text{H}_{\text{tot}})_{\text{obs}} - \log(X/\text{H})_{\odot} \quad (7)$$

is the observed depletion of element X . Since the quantities A_X , B_X , and z_X have been tabulated for many different elements, a least-squares linear fit to the equation:

$$y = a + bx, \quad (8)$$

where

$$y = [\text{X}/\text{H}]_{\text{obs}} - B_X + A_X z_X \quad (9)$$

and

$$x = A_X, \quad (10)$$

will yield values for the coefficients

$$a = [\text{M}/\text{H}]_{\text{ISM}} \quad (11)$$

and

$$b = F_*. \quad (12)$$

As stated above, the metallicity derived in this way is the metallicity of the absorption system relative to the average ISM metallicity in the solar neighborhood. It is *not* the metallicity relative to an adopted solar (or cosmic) abundance standard. To see why this is the case, let us consider the definition of the intercept parameter B_X . Rearranging Equation (2) and setting $F_* = z_X$ gives:

$$B_X = [\text{X}/\text{H}]_{F_* = z_X} = \log(X/\text{H})_{F_* = z_X} - \log(X/\text{H})_{\odot}, \quad (13)$$

where $\log(X/\text{H})_{F_* = z_X}$ is the (average) logarithmic abundance of element X evaluated at $F_* = z_X$ (according to the linear fit used to determine A_X and B_X). Substituting the above expression for B_X into Equation (6) and rearranging terms yields:

$$[\text{M}/\text{H}]_{\text{ISM}} = \log(X/\text{H})_{\text{obs}} - \log(X/\text{H})_{F_* = z_X} - A_X(F_* - z_X). \quad (14)$$

Note that Equation (14) makes no reference to any solar (or cosmic) abundance standard. The terms involving the solar abundance of element X have cancelled out of the equation. Nevertheless, despite this apparent shortcoming, the method described here can still provide us with useful information on the variations in metallicity that characterize the interstellar gas in the solar vicinity. In Section 4, we use this method to derive relative ISM metallicities for a sample of 84 sight lines probing the local Galactic ISM.

3. CONSTRUCTING THE SAMPLE

In order to obtain a statistically significant result for the metallicity distribution in the solar neighborhood, we need high-quality column density measurements for a variety of elements in their dominant ionization stage for a relatively large sample of interstellar sight lines. Fortunately, many such measurements have been published over the past several decades. Thus, in constructing our sample, we rely primarily on column density measurements reported in the literature (Section 3.1). However, we supplement these data with new column density determinations for certain key elements and for several important and/or interesting sight lines (as described in Section 3.2).

3.1. Accumulation of Data from the Literature

In compiling our database of high-quality column density measurements from the literature, we focus on the

following elements: B, C, N, O, Mg, Si, P, Cl, Ti, Cr, Mn, Fe, Ni, Cu, Zn, Ga, Ge, As, Kr, Cd, Sn, and Pb. All 22 of these elements have been analyzed in a way consistent with the methodology devised by Jenkins (2009), and all have values of the depletion parameters A_X , B_X , and z_X tabulated in the literature (Jenkins 2009; Ritchey et al. 2018, 2023).¹ The inclusion of as many different elements as possible in our least-squares linear fits helps to ensure that the relative ISM metallicities we derive are robust.

Most of the dominant ions of the elements listed above have electronic transitions out of the ground state with wavelengths in the UV portion of the spectrum accessible to the Hubble Space Telescope (HST). For these ions, we restricted our search to determinations of column densities based on observations obtained with the Space Telescope Imaging Spectrograph (STIS) or the Goddard High Resolution Spectrograph (GHRS). We do not include in our sample measurements made using earlier spaceborne instruments such as Copernicus or the International Ultraviolet Explorer. Abundance determinations made using these earlier UV instruments

tend to be less precise than those based on HST observations (e.g., Meyer et al. 1998). For a few ions (e.g., N I, Cl II, and Fe II), many of the observed transitions have wavelengths below 1200 Å, a regime covered by the Far Ultraviolet Spectroscopic Explorer (FUSE). Finally, all of the observed transitions of Ti II have wavelengths above 3000 Å. A variety of ground-based optical telescopes have been used to study these transitions (see, e.g., Welty & Crowther 2010).

Many investigations of elemental abundances based on observations of interstellar absorption lines fall into one of two categories. Some studies focus on one or several elements and obtain abundances for a large, diverse set of interstellar sight lines (e.g., Cartledge et al. 2004, 2006; Ritchey et al. 2011, 2018, 2023; Jenkins 2019). Others focus on a single line of sight and derive abundances for as many atomic (and molecular) species as possible (e.g., Sonneutrucker et al. 2002, 2003; Welty et al. 2020). Both types of investigations are utilized in the present study, where our aim is to compile as many reliable elemental abundance measurements as possible for as large a sample as is feasible.

Table 1. Stellar and Sight Line Properties for the Final Sample

Star	Name	Sp. Type	V	$E(B-V)$	l	b	d^a	z	$\log N(\text{H}_{\text{tot}})$	Ref. ^b
			(mag)	(mag)	(deg)	(deg)	(kpc)	(kpc)		
HD 1383	...	B1II	7.63	0.47	119.02	-0.89	$2.50^{+0.18}_{-0.13}$	-0.039	$21.54^{+0.04}_{-0.05}$	1
HD 12323	...	ON9.2V	8.92	0.23	132.91	-5.87	$2.44^{+0.23}_{-0.22}$	-0.250	$21.28^{+0.04}_{-0.04}$	1
HD 13268	...	ON8.5IIIIn	8.18	0.36	133.96	-4.99	$1.77^{+0.09}_{-0.07}$	-0.154	$21.44^{+0.06}_{-0.07}$	1
HD 13745	V354 Per	O9.7IIIn	7.90	0.46	134.58	-4.96	$2.28^{+0.15}_{-0.09}$	-0.197	$21.46^{+0.04}_{-0.05}$	1
HD 14434	...	O5.5Vnfp	8.49	0.48	135.08	-3.82	$2.24^{+0.10}_{-0.09}$	-0.150	$21.47^{+0.07}_{-0.09}$	2
HD 15137	...	O9.5II-IIIIn	7.86	0.35	137.46	-7.58	$2.05^{+0.17}_{-0.13}$	-0.271	$21.32^{+0.07}_{-0.08}$	1
HD 23180	<i>o</i> Per	B1III	3.83	0.30	160.36	-17.74	$0.341^{+0.052}_{-0.040}$	-0.104	$21.19^{+0.10}_{-0.14}$	2
HD 24190	...	B2Vn	7.45	0.30	160.39	-15.18	$0.375^{+0.005}_{-0.005}$	-0.098	$21.30^{+0.05}_{-0.06}$	2
HD 24398	ζ Per	B1Ib	2.85	0.34	162.29	-16.69	$0.264^{+0.022}_{-0.022}$	-0.076	$21.19^{+0.06}_{-0.08}$	2
HD 24534	X Per	O9.5III	6.72	0.59	163.08	-17.14	$0.596^{+0.017}_{-0.014}$	-0.176	$21.34^{+0.03}_{-0.04}$	2
HD 24912	ξ Per	O7.5IIInf	4.06	0.35	160.37	-13.11	$0.418^{+0.058}_{-0.039}$	-0.095	$21.29^{+0.08}_{-0.09}$	2
HD 35149	23 Ori	B1Vn	5.00	0.11	199.16	-17.86	$0.575^{+0.119}_{-0.078}$	-0.176	$20.74^{+0.08}_{-0.10}$	3
HD 37021	θ ¹ Ori B	B3V	7.96	0.48	209.01	-19.38	$0.375^{+0.005}_{-0.006}$	-0.124	$21.65^{+0.13}_{-0.19}$	2
HD 37061	NU Ori	B0.5V	6.83	0.56	208.92	-19.27	$0.409^{+0.011}_{-0.010}$	-0.135	$21.73^{+0.09}_{-0.11}$	2

Table 1 continued

¹ While Jenkins (2009) determined depletion parameters for S, he pointed out difficulties in working with that element. The only S II transitions that are available are the ones in the strong triplet that spans 1250 to 1260 Å. For most sight lines, these absorption features are strongly saturated. When the total hydrogen column density is low enough, the lines are not saturated, but contributions of S II from H II regions can lead to misleading conclusions on the abundance of S in the neutral gas.

Table 1 (continued)

Star	Name	Sp. Type	V	$E(B-V)$	l	b	d^a	z	$\log N(\text{H}_{\text{tot}})$	Ref. ^b
			(mag)	(mag)	(deg)	(deg)	(kpc)	(kpc)		
HD 37903	...	B1.5V	7.83	0.35	206.85	-16.54	$0.394^{+0.003}_{-0.004}$	-0.112	$21.44^{+0.06}_{-0.07}$	2
HD 52266	...	O9.5IIIIn	7.23	0.29	219.13	-0.68	$1.35^{+0.06}_{-0.07}$	-0.016	$21.27^{+0.04}_{-0.04}$	1
HD 53975	...	O7.5Vz	6.50	0.21	225.68	-2.32	$1.12^{+0.07}_{-0.06}$	-0.045	$21.09^{+0.04}_{-0.04}$	1
HD 57061	τ CMa	O9II	4.40	0.16	238.18	-5.54	$3.22^{+1.79}_{-1.41}$	-0.311	$20.70^{+0.04}_{-0.04}$	2
HD 62542	...	B5V	8.03	0.35	255.92	-9.24	$0.366^{+0.002}_{-0.002}$	-0.059	$21.25^{+0.17}_{-0.28}$	4
HD 63005	...	O7Vf	9.13	0.27	242.47	-0.93	$3.72^{+0.60}_{-0.50}$	-0.060	$21.31^{+0.03}_{-0.03}$	1
HD 69106	...	B0.2V	7.13	0.20	254.52	-1.33	$1.42^{+0.10}_{-0.06}$	-0.033	$21.11^{+0.04}_{-0.04}$	1
HD 73882	NX Vel	O8.5IV	7.19	0.70	260.18	+0.64	$0.737^{+0.031}_{-0.030}$	+0.008	$21.57^{+0.08}_{-0.09}$	2
HD 75309	...	B1IIp	7.84	0.29	265.86	-1.90	$1.82^{+0.12}_{-0.13}$	-0.060	$21.19^{+0.03}_{-0.03}$	1
HD 79186	GX Vel	B5Ia	5.00	0.40	267.36	+2.25	$1.81^{+0.34}_{-0.23}$	+0.071	$21.41^{+0.07}_{-0.08}$	2
HD 88115	...	B1.5IIn	9.36	0.16	285.32	-5.53	$2.53^{+0.16}_{-0.17}$	-0.243	$21.04^{+0.06}_{-0.07}$	1
HD 90087	...	O9.2III	8.92	0.28	285.16	-2.13	$2.19^{+0.11}_{-0.12}$	-0.082	$21.23^{+0.05}_{-0.05}$	1
HD 91824	...	O7Vfz	8.14	0.24	285.70	+0.07	$1.83^{+0.08}_{-0.08}$	+0.002	$21.16^{+0.04}_{-0.04}$	1
HD 91983	...	B1III	8.55	0.29	285.88	+0.05	$2.40^{+0.15}_{-0.14}$	+0.002	$21.22^{+0.05}_{-0.06}$	1
HD 92554	...	O9.5IIIn	10.15	0.39	287.60	-2.02	$4.04^{+0.31}_{-0.28}$	-0.142	$21.35^{+0.09}_{-0.11}$	1
HD 93205	V560 Car	O3.5V	7.75	0.38	287.57	-0.71	$2.25^{+0.12}_{-0.11}$	-0.028	$21.38^{+0.05}_{-0.05}$	1
HD 93222	...	O7IIIIf	8.10	0.36	287.74	-1.02	$2.41^{+0.14}_{-0.15}$	-0.043	$21.49^{+0.03}_{-0.03}$	1
HD 94493	...	B1Ib	7.59	0.23	289.01	-1.18	$2.15^{+0.14}_{-0.12}$	-0.044	$21.18^{+0.05}_{-0.06}$	1
HD 99857	...	B0.5Ib	7.49	0.35	294.78	-4.94	$1.80^{+0.08}_{-0.07}$	-0.155	$21.35^{+0.06}_{-0.07}$	1
HD 99890	...	B0IIIIn	9.26	0.24	291.75	+4.43	$2.53^{+0.18}_{-0.17}$	+0.195	$21.14^{+0.05}_{-0.05}$	1
HD 104705	DF Cru	B0Ib	9.11	0.23	297.45	-0.34	$1.94^{+0.16}_{-0.15}$	-0.011	$21.21^{+0.05}_{-0.06}$	1
HD 108639	...	B0.2III	8.57	0.37	300.22	+1.95	$1.98^{+0.10}_{-0.11}$	+0.067	$21.40^{+0.04}_{-0.04}$	1
HD 114886	...	O9III	6.89	0.40	305.52	-0.83	$1.83^{+0.95}_{-0.78}$	-0.026	$21.41^{+0.05}_{-0.06}$	1
HD 116781	V967 Cen	B0IIIIne	7.62	0.43	307.05	-0.07	$2.11^{+0.15}_{-0.13}$	-0.002	$21.27^{+0.05}_{-0.05}$	1
HD 116852	...	O8.5II-IIIIf	8.47	0.21	304.88	-16.13	$3.42^{+0.39}_{-0.32}$	-0.949	$21.01^{+0.04}_{-0.04}$	1
HD 121968	...	B1V	10.26	0.07	333.97	+55.84	$3.94^{+0.91}_{-0.63}$	+3.263	$20.59^{+0.12}_{-0.16}$	2
HD 122879	...	B0Ia	6.50	0.36	312.26	+1.79	$2.22^{+0.16}_{-0.13}$	+0.069	$21.39^{+0.05}_{-0.06}$	1
HD 124314	...	O6IVnf	6.64	0.53	312.67	-0.42	$1.61^{+0.11}_{-0.10}$	-0.012	$21.49^{+0.05}_{-0.06}$	1
HD 137595	...	B3Vn	7.49	0.25	336.72	+18.86	$0.751^{+0.021}_{-0.022}$	+0.243	$21.23^{+0.04}_{-0.05}$	1
HD 141637	1 Sco	B2.5Vn	4.64	0.15	346.10	+21.71	$0.147^{+0.003}_{-0.003}$	+0.054	$21.13^{+0.10}_{-0.13}$	2
HD 147683	V760 Sco	B4V+B4V	7.05	0.39	344.86	+10.09	$0.290^{+0.002}_{-0.002}$	+0.051	$21.41^{+0.11}_{-0.14}$	2
HD 147888	ρ Oph D	B3V	6.74	0.47	353.65	+17.71	$0.124^{+0.006}_{-0.006}$	+0.038	$21.73^{+0.07}_{-0.09}$	1
HD 147933	ρ Oph A	B2V	5.05	0.45	353.69	+17.69	$0.137^{+0.003}_{-0.003}$	+0.042	$21.70^{+0.08}_{-0.10}$	2
HD 148937	...	O6f?p	6.71	0.65	336.37	-0.22	$1.15^{+0.03}_{-0.03}$	-0.004	$21.60^{+0.05}_{-0.05}$	1
HD 149404	V918 Sco	O8.5Iabfp	5.52	0.68	340.54	+3.01	$1.30^{+0.13}_{-0.11}$	+0.068	$21.57^{+0.10}_{-0.13}$	5, 6
HD 149757	ζ Oph	O9.5IVnn	2.56	0.32	6.28	+23.59	$0.139^{+0.017}_{-0.015}$	+0.055	$21.15^{+0.03}_{-0.03}$	2
HD 152590	V1297 Sco	O7.5Vz	9.29	0.48	344.84	+1.83	$1.68^{+0.08}_{-0.06}$	+0.053	$21.47^{+0.06}_{-0.07}$	1
HD 157857	...	O6.5IIIIf	7.78	0.43	12.97	+13.31	$2.22^{+0.20}_{-0.13}$	+0.511	$21.44^{+0.07}_{-0.08}$	2
HD 165246	...	O8Vn	7.60	0.38	6.40	-1.56	$1.19^{+0.04}_{-0.05}$	-0.032	$21.45^{+0.03}_{-0.03}$	1
HD 165955	...	B3Vn	9.59	0.15	357.41	-7.43	$1.47^{+0.12}_{-0.09}$	-0.190	$21.11^{+0.06}_{-0.07}$	2, 7

Table 1 continued

Table 1 (continued)

Star	Name	Sp. Type	V	$E(B-V)$	l	b	d^a	z	$\log N(\text{H}_{\text{tot}})$	Ref. ^b
			(mag)	(mag)	(deg)	(deg)	(kpc)	(kpc)		
HD 170740	...	B2IV-V	5.72	0.48	21.06	-0.53	$0.225^{+0.005}_{-0.005}$	-0.002	$21.43^{+0.05}_{-0.06}$	1
HD 177989	...	B0III	9.34	0.23	17.81	-11.88	$2.41^{+0.20}_{-0.19}$	-0.496	$21.10^{+0.05}_{-0.05}$	1
HD 185418	...	B0.5V	7.49	0.50	53.60	-2.17	$0.692^{+0.010}_{-0.009}$	-0.026	$21.41^{+0.04}_{-0.05}$	1
HD 191877	...	B1Ib	6.27	0.21	61.57	-6.45	$1.73^{+0.11}_{-0.13}$	-0.194	$21.10^{+0.05}_{-0.06}$	1
HD 192035	RX Cyg	B0III-IVn	8.22	0.34	83.33	+7.76	$1.65^{+0.06}_{-0.06}$	+0.223	$21.39^{+0.04}_{-0.05}$	1
HD 192639	...	O7.5Iab	7.11	0.66	74.90	+1.48	$1.81^{+0.07}_{-0.06}$	+0.047	$21.48^{+0.07}_{-0.08}$	2
HD 195455	...	B0.5III	9.20	0.10	20.27	-32.14	$2.35^{+0.35}_{-0.24}$	-1.251	$20.62^{+0.04}_{-0.04}$	1
HD 195965	...	B0V	6.97	0.25	85.71	+5.00	$0.790^{+0.023}_{-0.025}$	+0.069	$21.08^{+0.04}_{-0.05}$	1
HD 198478	55 Cyg	B3Ia	4.86	0.57	85.75	+1.49	$1.84^{+0.35}_{-0.22}$	+0.048	$21.51^{+0.16}_{-0.26}$	1
HD 201345	...	ON9.2IV	7.76	0.15	78.44	-9.54	$1.83^{+0.15}_{-0.11}$	-0.303	$21.02^{+0.05}_{-0.05}$	1
HD 202347	...	B1.5V	7.50	0.17	88.22	-2.08	$0.764^{+0.023}_{-0.019}$	-0.028	$20.94^{+0.07}_{-0.08}$	1
HD 203374	...	B0IVpe	6.67	0.53	100.51	+8.62	$2.04^{+1.42}_{-0.76}$	+0.306	$21.40^{+0.04}_{-0.05}$	1
HD 206267	...	O6Vf	5.62	0.53	99.29	+3.74	$0.790^{+0.172}_{-0.112}$	+0.052	$21.49^{+0.05}_{-0.06}$	1
HD 206773	...	B0Vpe	6.87	0.45	99.80	+3.62	$0.888^{+0.016}_{-0.014}$	+0.056	$21.24^{+0.05}_{-0.06}$	1
HD 207198	...	O8.5II	5.94	0.62	103.14	+6.99	$0.978^{+0.034}_{-0.027}$	+0.119	$21.50^{+0.05}_{-0.05}$	1
HD 207308	...	B0.5V	7.49	0.53	103.11	+6.82	$0.906^{+0.017}_{-0.013}$	+0.108	$21.45^{+0.04}_{-0.05}$	1
HD 207538	...	O9.7IV	7.30	0.64	101.60	+4.67	$0.830^{+0.013}_{-0.013}$	+0.068	$21.52^{+0.04}_{-0.05}$	1
HD 208440	...	B1V	7.91	0.28	104.03	+6.44	$0.877^{+0.019}_{-0.018}$	+0.098	$21.33^{+0.05}_{-0.06}$	1
HD 209339	...	O9.7IV	8.51	0.36	104.58	+5.87	$0.936^{+0.028}_{-0.024}$	+0.096	$21.27^{+0.04}_{-0.04}$	1
HD 210809	...	O9Iab	7.56	0.31	99.85	-3.13	$3.66^{+0.52}_{-0.34}$	-0.200	$21.35^{+0.06}_{-0.06}$	1
HD 210839	λ Cep	O6.5Infp	5.05	0.57	103.83	+2.61	$0.833^{+0.066}_{-0.049}$	+0.038	$21.48^{+0.04}_{-0.04}$	1
HD 212791	V408 Lac	B3ne	8.02	0.17	101.64	-4.30	$0.893^{+0.019}_{-0.016}$	-0.067	$21.13^{+0.12}_{-0.16}$	2
HD 218915	...	O9.2Iab	7.20	0.30	108.06	-6.89	$2.97^{+0.33}_{-0.25}$	-0.357	$21.27^{+0.06}_{-0.07}$	1
HD 219188	...	B0.5IIIn	7.06	0.13	83.03	-50.17	$2.10^{+0.25}_{-0.27}$	-1.611	$20.76^{+0.07}_{-0.08}$	1
HD 220057	...	B3IV	6.94	0.23	112.13	+0.21	$0.385^{+0.004}_{-0.004}$	+0.001	$21.10^{+0.11}_{-0.14}$	1
HD 224151	V373 Cas	B0.5II-III	6.00	0.44	115.44	-4.64	$1.89^{+0.13}_{-0.10}$	-0.153	$21.47^{+0.04}_{-0.05}$	1
HDE 232522	...	B1II	8.70	0.27	130.70	-6.71	$3.46^{+0.41}_{-0.44}$	-0.404	$21.21^{+0.04}_{-0.04}$	1
HDE 303308	...	O4.5Vfc	8.17	0.45	287.59	-0.61	$2.17^{+0.09}_{-0.10}$	-0.023	$21.46^{+0.03}_{-0.03}$	1
HDE 308813	...	O9.7IVn	9.73	0.34	294.79	-1.61	$2.43^{+0.11}_{-0.09}$	-0.068	$21.28^{+0.05}_{-0.06}$	1
CPD-59 2603	V572 Car	O7Vnz	8.81	0.46	287.59	-0.69	$2.63^{+0.16}_{-0.14}$	-0.032	$21.46^{+0.04}_{-0.04}$	1

^aDistances are based on Gaia EDR3 parallax measurements (Bailer-Jones et al. 2021).

^bReference(s) for the values of $N(\text{H I})$ and $N(\text{H}_2)$ used to calculate $N(\text{H}_{\text{tot}})$: (1) Jenkins (2019); (2) Jenkins (2009); (3) Welty et al. (1999); (4) Welty et al. (2020); (5) Diplas & Savage (1994); (6) Rachford et al. (2009); (7) Ritchey et al. (2023).

After our initial survey of the literature, our database contained column density measurements for the dominant ions of the elements listed above for a total of 223 sight lines. All of these measurements (with the exception of those for Ti II) are based on spectroscopic observations acquired using HST or FUSE. However, approximately half of the sight lines in this initial database had abundance measurements for only a few elements. In

order for the method described in Section 2 to yield reliable determinations of $[\text{M}/\text{H}]_{\text{ISM}}$, each sight line should have a sufficient number of elemental abundance measurements, and the elements measured should have as wide a range as possible of A_X values, so that the slopes and y -intercepts of the linear fits are adequately constrained. We decided (somewhat arbitrarily) that each sight line should have abundance measurements for at least eight different elements in order to be included in

our survey. The imposition of this threshold left us with a sample of 78 sight lines. (Six sight lines with the requisite number of column density measurements were excluded from our survey because they do not have published and/or reliable values of $N(\text{H I})$ and $N(\text{H}_2)$ necessary for the metallicity analysis.) Six additional sight lines were subsequently added to our sample based on new column density measurements (as described in Section 3.2) bringing the total number of sight lines in our final sample to 84.

Basic information regarding the background stars and the characteristics of the sight lines included in the final sample is provided in Table 1. The stellar distances and their uncertainties (as well as the values of z derived from the distances) are based on Gaia EDR3 parallax measurements (Bailer-Jones et al. 2021). Most of the measurements of $N(\text{H I})$ and $N(\text{H}_2)$ used to derive $N(\text{H}_{\text{tot}})$ are obtained from Jenkins (2019) or from the values compiled by Jenkins (2009). Exceptions to this are noted in the table. A compilation of column density measurements for all of the elements other than hydrogen for the 84 sight lines in our final sample is provided in the appendix.

Table 2. Wavelengths and Oscillator Strengths

Species	λ^a (Å)	$\log f\lambda$	Error ^b (dex)	Ref.
B II	1362.463	3.133	0.002	1
C II	1334.532	2.234	...	1
	2325.403	-3.954	0.003	1
N I	951.079	-0.795	...	1
	951.295	-1.656	...	1
	953.415	1.091	...	1
	953.655	1.372	...	1
	959.494	-1.304	...	1
	1134.165	1.219	...	1
	1134.415	1.512	...	1
	1134.980	1.674	...	1
	1159.817	-1.938	...	1
	1160.937	-2.496	...	1
	1199.550	2.199	...	1
	1200.223	2.018	...	1
	1200.710	1.715	...	1
O I	1355.598	-2.805	...	1
Mg II	1239.925	-0.106	...	1
	1240.395	-0.355	...	1

Table 2 continued

Table 2 (*continued*)

Species	λ^a (Å)	$\log f\lambda$	Error ^b (dex)	Ref.
	2796.354	3.236	0.004	1
	2803.532	2.933	0.003	1
Si II	1808.013	0.575	0.040	1
	2335.123	-2.003	0.080	1
P II	1152.818	2.496	0.044	2
	1301.874	1.407	0.042	3
	1532.533	1.053	0.044	4
Cl I	1004.678	1.677	0.032	5
	1094.769	1.625	0.012	5
	1097.369	0.985	0.070	1
	1347.240	2.314	0.030	1
	1379.528	0.569	...	6
Cl II	1071.036	1.182	0.021	7
Ti II	3072.970	2.571	0.027	1
	3229.190	2.346	0.026	1
	3241.983	2.876	0.027	1
	3383.759	3.084	0.034	1
Cr II	2056.257	2.326	0.024	1
	2062.236	2.194	0.023	1
	2066.164	2.024	0.025	1
Mn II	1197.184	2.248	...	8
	1199.391	2.143	...	8
	1201.118	2.004	...	8
	2305.714	0.423	0.050	1
	2576.877	2.969	0.006	1
	2594.499	2.860	0.020	1
	2606.462	2.712	0.021	1
Fe II	1055.262	0.812	...	1
	1112.048	0.695	...	1
	1121.975	1.512	...	1
	1125.448	1.244	...	1
	1127.098	0.102	...	1
	1133.665	0.728	...	1
	1142.366	0.661	...	1
	1143.226	1.342	...	1
	1144.938	1.978	0.030	1
	1608.451	1.968	0.026	1
	1611.201	0.347	0.080	1
	2234.447	-1.540	0.050	9
	2249.877	0.612	0.030	1

Table 2 continued

Table 2 (*continued*)

Species	λ^a (Å)	$\log f\lambda$	Error ^b (dex)	Ref.
	2260.781	0.742	0.030	1
	2344.214	2.427	0.008	1
	2367.591	-0.713	0.072	9
	2374.461	1.871	0.020	1
	2382.765	2.882	0.005	1
Ni II	1317.217	1.876	0.043	10
	1370.132	1.906	0.042	10
	1454.842	1.505	0.029	11
	1709.604	1.735	0.024	11
	1741.553	1.876	0.024	11
	1751.916	1.691	0.023	11
	1804.473	0.919	0.053	11
Cu II	1358.773	2.569	0.042	12
Zn II	2026.137	3.007	0.030	1
	2062.660	2.706	0.030	1
Ga II	1414.402	3.399	0.020	1
Ge II	1237.059	3.033	0.053	13
	1602.486	2.362	...	14
As II	1263.770	2.515	...	14
Kr I	1164.867	2.341	0.004	14
	1235.838	2.402	0.004	14
Cd II	2145.070	3.029	0.011	14
	2265.715	2.749	0.006	14
Sn II	1400.440	3.158	0.040	14
Pb II	1203.616	2.956	0.017	15
	1433.906	2.663	0.044	15

^aWavelengths are specified in vacuum except those for Ti II, which are specified in air.

^bUncertainty in the value of $\log f\lambda$. Transitions with no uncertainties listed are derived from theoretical calculations.

References—(1) Morton (2003), (2) Federman et al. (2007), (3) Brown et al. (2018), (4) Ritchey et al. (2023), (5) Alkhayat et al. (2019), (6) Oliver & Hibbert (2013), (7) Schectman et al. (2005), (8) Toner & Hibbert (2005), (9) Miller et al. (2007), (10) Jenkins & Tripp (2006), (11) Boissé & Bergeron (2019), (12) Brown et al. (2009), (13) Heidarian et al. (2017), (14) Morton (2000), (15) Heidarian et al. (2015).

All of the column densities in our final compilation were adjusted so that they correspond to a common set of oscillator strengths (f -values). An exhaustive

list of the transitions used by various authors to derive the column densities included in the present investigation is provided in Table 2. Most of the f -values adopted in the present work are from the compilations of Morton (2000, 2003). However, there have been several significant improvements in oscillator strengths in the two decades since those compilations were published. New experimental f -values are now available for commonly observed transitions of P II (Federman et al. 2007; Brown et al. 2018), Cl I (Alkhayat et al. 2019), Cl II (Schectman et al. 2005), Cu II (Brown et al. 2009), Ge II (Heidarian et al. 2017), and Pb II (Heidarian et al. 2015). In addition, empirically-derived f -values have been determined for several transitions of Fe II (Miller et al. 2007) and Ni II (Jenkins & Tripp 2006; Boissé & Bergeron 2019). There are no experimentally-determined f -values for the Mn II $\lambda\lambda$ 1197, 1199, 1201 triplet. Following Cashman et al. (2017), we adopt the theoretical results of Toner & Hibbert (2005) for these Mn II lines. Finally, while there are new theoretical calculations for the oscillator strengths of the Ti II λ 3072, λ 3229, λ 3241, and λ 3383 lines (Lundberg et al. 2016), and the Zn II $\lambda\lambda$ 2026, 2062 doublet (Kisielius et al. 2015), we prefer the experimental f -values listed in Morton (2003) for these transitions.²

In Table 3, we present the complete list of references that supplied column densities for the metallicity analysis, along with a code for each reference. These codes are used in the appendix to identify the source of each column density measurement. We also indicate for each reference in Table 3 the element or elements from that investigation whose column densities are included in the present study. If the column density measurements pertain to just a single line of sight, then the sight line is also indicated. It is important to note that, while over 40 references are listed in Table 3, approximately two-thirds of the more than 900 column density measurements in our final sample come from just six references: Cartledge et al. (2006), Jensen & Snow (2007), Ritchey et al. (2011, 2018, 2023), and Jenkins (2019). Another 12% of the measurements are newly derived column densities obtained in this work (Section 3.2). Finally, many of the column density measurements adopted for the line of sight toward HD 24534

² The adopted f -values often have little impact on the metallicity analysis. If all of the column densities for a certain element are derived from one transition (or a particular set of transitions) and the f -value of that transition is altered, the column densities will be shifted accordingly. However, the B_X parameter will also be shifted in the opposite sense, leaving the values of y for that element unchanged (see Equation 9).

Table 3. Reference Codes for Column Density Measurements

Code	Reference	Elements Included in the Present Study
A++03	André et al. (2003)	O
C++91	Cardelli et al. (1991a)	O, Mg, P, Cr, Mn, Fe, Ni, Cu, Zn (ξ Per)
CSE91	Cardelli et al. (1991b)	Ge (ξ Per)
CMES93	Cardelli et al. (1993a)	C (ζ Oph)
CFLT93	Cardelli et al. (1993b)	As (ζ Oph)
C94	Cardelli (1994)	Pb (ζ Oph)
C++94	Cardelli et al. (1994)	Si (ζ Oph)
CMJS96	Cardelli et al. (1996)	C (ζ Per)
CM97	Cardelli & Meyer (1997)	Kr
CMLS01	Cartledge et al. (2001)	O
CML03	Cartledge et al. (2003)	Kr
CLMS04	Cartledge et al. (2004)	O
CLMS06	Cartledge et al. (2006)	Mg, P, Mn, Ni, Cu, Ge
C++08	Cartledge et al. (2008)	O, Kr
F++03	Federman et al. (2003)	Ga (ρ Oph A)
H++93	Hobbs et al. (1993)	Cu, Ga, Ge, Kr (1 Sco)
J19	Jenkins (2019)	O, Mg, Mn, Ge, Kr
JRS07	Jensen et al. (2007)	N
JS07	Jensen & Snow (2007)	Fe
KAMM03	Knauth et al. (2003)	N
KML06	Knauth et al. (2006)	N
L++98	Lambert et al. (1998)	B (ζ Oph)
MJC98	Meyer et al. (1998)	O (τ CMa)
M++07	Miller et al. (2007)	Si, Fe
RFSL11	Ritchey et al. (2011)	B, O, Cu, Ga
RFL18	Ritchey et al. (2018)	B, O, Ga, Ge, As, Kr, Cd, Sn, Pb
R*	This work	C, O, Mg, Si, Ti, Cr, Mn, Fe, Ni, Cu, Ge, As, Kr, Cd, Pb
R**	Ritchey (in preparation)	C, N, Mg, Si, Cr, Mn, Fe, Ni, Zn (X Per)
RBFS23	Ritchey et al. (2023)	P, Cl
RB95	Roth & Blades (1995)	Cr, Zn
SCS92	Savage et al. (1992)	N, O, Mg, Cr, Mn, Fe, Ni, Cu, Ga, Ge, Kr (ζ Oph)
SS96a	Sembach & Savage (1996)	Cr, Fe, Zn (HD 116852)
SS96b	Savage & Sembach (1996)	P, Zn (ζ Oph)
SRF02	Snow et al. (2002)	Fe
SCS94	Sofia et al. (1994)	Si (ζ Oph)
SCGM97	Sofia et al. (1997)	C (τ CMa)
SMC99	Sofia et al. (1999)	Cd, Sn
SLMC04	Sofia et al. (2004)	C
S++02	Sonnentrucker et al. (2002)	O, Mg, Mn, Fe, Ni, Cu (HD 192639)
S++03	Sonnentrucker et al. (2003)	N, Mg, Mn, Fe, Ni (HD 185418)
W++95	Welty et al. (1995)	Pb (1 Sco)
W++99	Welty et al. (1999)	C, N, O, Mg, Si, P, Cr, Mn, Fe, Ni, Cu, Zn, Ga, Ge, Sn (23 Ori)
W07	Welty (2007)	O, Mg, Mn, Fe, Ni, Cu, Ge (HD 219188)
WC10	Welty & Crowther (2010)	Ti
WSSY20	Welty et al. (2020)	O, Mg, Si, P, Fe, Ni, Cu, Zn, Ga, Ge, Kr, Cd, Sn (HD 62542)
W*	Welty (2022, private communication)	Ge (HD 192639)

(X Per) are from an unpublished survey of atomic and molecular abundances in that direction (A. M. Ritchey, in preparation).

3.2. *New Column Density Determinations*

Once our literature survey was complete, we recognized that there were deficiencies in the abundance data available, especially for the refractory elements Ni and Ti. These elements are particularly important in the metallicity analysis because they represent two of the most severely depleted elements. With large (negative) values of the depletion slope parameter A_X , these elements help to anchor the least-squares linear fits used to derive values of $[M/H]_{\text{ISM}}$ (see Section 4). However, fewer than half of the sight lines in our sample drawn from the literature had published Ni II column densities (e.g., from [Cartledge et al. 2006](#)), while only about one-third had published measurements of Ti II (see [Welty & Crowther 2010](#)). This is despite the fact that Ni II observations are available from the Mikulski Archive for Space Telescopes (MAST) for nearly every sight line in our sample (due to the prevalence of STIS E140H spectra obtained with the 1271 Å central wavelength setting). Furthermore, nearly half of our sight lines have archival ground-based spectra obtained with the Ultraviolet and Visual Echelle Spectrograph (UVES) on the Very Large Telescope (VLT) that cover the relevant Ti II transitions between 3200 Å and 3400 Å. We therefore decided to derive Ni II column densities for all of the sight lines in our sample lacking this measurement for which high-resolution STIS echelle spectra are available in the MAST archive and Ti II column densities for all of our sight lines with archival VLT/UVES data.

High-resolution (E140H and E230H) STIS spectra were obtained from the MAST archive for all central wavelength settings that cover the Ni II $\lambda 1317$, $\lambda 1370$, $\lambda 1454$, $\lambda 1709$, $\lambda 1741$, and $\lambda 1751$ transitions. (These data have velocity resolutions in the range 2.1–3.7 km s⁻¹.) Multiple exposures of the same star were co-added and the overlapping portions of the echelle orders were combined. Portions of the spectra surrounding the Ni II absorption lines were normalized to the continuum via low-order Legendre polynomial fits. Column densities were obtained from individual Ni II transitions by integrating the apparent optical depth (AOD) profiles (e.g., [Savage & Sembach 1991](#); [Jenkins 2019](#)). Uncertainties in the AOD column densities were calculated by adding in quadrature the uncertainties arising from noise in the spectra, from errors in continuum placement, and from uncertainties in the adopted values of $\log f\lambda$. Final Ni II column densities were obtained by

taking a weighted mean of the results derived from the different transitions along a given line of sight.

Pipeline-processed VLT/UVES spectra covering the Ti II $\lambda 3229$, $\lambda 3241$, and $\lambda 3383$ transitions were downloaded from the European Southern Observatory (ESO) Science Archive Facility. (The UVES spectra have a nominal velocity resolution of ~ 4.2 km s⁻¹.) Multiple exposures of a given target were weighted according to the signal-to-noise (S/N) ratios of the spectra and co-added, after correcting the velocity scales to the reference frame of the local standard of rest (LSR). Column densities (and uncertainties in column density) were obtained using the AOD method, as discussed above for the Ni II lines. When multiple Ti II transitions were detected in a given direction, final column densities were derived from a weighted mean of the results obtained from the individual transitions.

Most of the Ni II and Ti II lines examined here do not show significant evidence of unresolved saturated absorption in the line profiles. The results obtained from different transitions of the same ion along the same line of sight generally agree within the uncertainties. For HD 79186 and HD 149757 (ζ Oph), however, there are significant discrepancies in the column densities derived from the Ti II $\lambda 3383$ and $\lambda 3241$ lines. For these sight lines, we adopt the results from the stronger $\lambda 3383$ transition, which is less influenced by noise arising from CCD response fringes in the UVES data. For HD 37061, the Ni II $\lambda 1317$ line is the only Ni II transition available, and the line both is extremely narrow and has a central depth approaching zero. For this sight line, and for several others with narrow absorption features, we obtained Ni II column densities via multi-component Voigt profile fitting using the code ISMOD ([Sheffer et al. 2008](#)).

We also obtained new column density determinations from high-resolution STIS spectra for two other refractory elements: Fe and Cr. Most published values of Fe II column densities for sight lines in our sample come from a study that relied on low-resolution ($\Delta v \sim 18$ km s⁻¹) FUSE spectra ([Jensen & Snow 2007](#)). Likewise, the only previously published Cr abundances in our database were derived in a single study that analyzed archival GHRS spectra ([Roth & Blades 1995](#)). However, high-resolution STIS spectra covering the Fe II $\lambda 1611$, $\lambda 2249$, and $\lambda 2260$ transitions and the Cr II $\lambda\lambda 2056, 2062, 2066$ triplet are available for several sight lines without published abundances for these ions. We therefore obtained Fe II and Cr II column densities for these directions using our Voigt profile fitting technique. We also derived Mg II and Mn II column densities for several sight lines that had not been previously analyzed by [Cartledge et al. \(2006\)](#) or [Jenkins \(2019\)](#). These

results were obtained via profile fitting of the Mg II $\lambda\lambda 1239, 1240$ doublet and the Mn II $\lambda 1197$ and $\lambda 1201$ lines.

Two sight lines (HD 73882 and HD 149404) initially had only three elemental abundance measurements published in the literature (for N, Ti, and Fe; Knauth et al. 2003; Jensen et al. 2007; Jensen & Snow 2007; Welty & Crowther 2010). However, new high-resolution STIS spectra recently became publically available for these directions.³ Since these sight lines are also analyzed in De Cia et al. (2021), we wanted to perform an independent analysis of the metallicities in these directions. To accomplish this, we analyzed the O I $\lambda 1355$, Mg II $\lambda\lambda 1239, 1240$, Ni II $\lambda 1317$, Ni II $\lambda 1370$, Cu II $\lambda 1358$, and Ge II $\lambda 1237$ lines via profile fitting to obtain the total column densities of these ions along the lines of sight. Where multiple transitions were analyzed for a given ion, final column densities were again obtained by evaluating a weighted mean.

High-resolution STIS spectra are also available for the line of sight to HD 147933 (ρ Oph A), although, to our knowledge, these data have not yet been published. This is another important sight line that was included in the De Cia et al. (2021) sample. The high total hydrogen column density and intrinsically narrow velocity distribution of the gas toward ρ Oph A, combined with the FUV and NUV coverage of the available high-resolution STIS spectra, allow us to derive column densities for many different dominant ions in this direction. In particular, we obtained column densities through profile synthesis fits to the following lines: C II $\lambda 2325$, O I $\lambda 1355$, Mg II $\lambda\lambda 1239, 1240$, Si II $\lambda 2335$, Mn II $\lambda 2305$, Fe II $\lambda 2367$, Ni II $\lambda 1317$, Ge II $\lambda 1237$, As II $\lambda 1263$, Kr I $\lambda 1235$, Cd II $\lambda\lambda 2145, 2265$, and Pb II $\lambda 1203$. These measurements represent the first reported detections of the weak C II $\lambda 2325$ and Si II $\lambda 2335$ lines toward ρ Oph A.

After compiling our database of elemental abundance measurements, we noted a few cases where the abundances appeared to be outliers. The O I and Kr I abundances toward HD 195455 reported by Jenkins (2019) are much larger than would be expected based on measurements toward sight lines with similar (low) molecular hydrogen fractions. The sight line to HD 195455 (at $l = 20.3$, $b = -32.1$) probes the lower Galactic halo out to a distance 1.25 kpc below the Galactic plane. This sight line also exhibits an unusual pattern of elemental abundances in plots of y versus x (see Section 4). Thus, to provide an independent check on the

abundances in this direction, we derived new column densities through a profile fitting analysis of the O I $\lambda 1355$, Mg II $\lambda\lambda 1239, 1240$, Mn II $\lambda 1197$, Ni II $\lambda 1317$, Ge II $\lambda 1237$, and Kr I $\lambda 1235$ lines. We also found that the Ge II abundance toward HD 192639 reported by Sonnentrucker et al. (2002) was significantly larger than any other published measurement of Ge/H. A new column density determination for Ge II toward HD 192639 (D. E. Welty, 2022, private communication) yields an abundance that is more in line with expectations.

3.3. Properties of the Sight Lines

Our final sample consists of 84 sight lines that probe a diverse array of interstellar environments throughout the local part of the Milky Way Galaxy. The distances to the stars used as background targets range from 120 pc to 4.0 kpc, while the values of $E(B-V)$ range from 0.07 to 0.70. Most of the targets probe interstellar material in the Galactic midplane. However, four stars (HD 116852, HD 121968, HD 195455, and HD 219188) sample gas in the lower halo out to a maximum z distance of 3.3 kpc. Thirteen of the 84 stars in our sample were included in the surveys of translucent sight lines published by Rachford et al. (2002, 2009). Translucent sight lines are characterized by high visual extinction ($A_V \gtrsim 1$ mag) and typically have high molecular hydrogen fractions. On the opposite extreme, 22 sight lines in our final sample have less than 10% of their total hydrogen in molecular form. The diverse characteristics of the sight lines in our sample help to ensure that the distribution of metallicities we derive is fully representative of the ISM in the solar vicinity.

4. DERIVATION OF RELATIVE ISM METALLICITIES

Once the total column densities have been determined for a variety of different elements along a given line of sight, it is straightforward to apply the methodology described in Section 2 to derive the relative ISM metallicity $[M/H]_{\text{ISM}}$ from a least-squares linear fit to a plot of y versus x , where y and x are defined in Equations (9) and (10), respectively. The complete list of column density measurements used in our analysis of relative ISM metallicities is provided in the appendix. Values of the element-specific depletion parameters A_X , B_X , and z_X are compiled in Table 4 for the 22 elements considered in our investigation. Note that the solar system abundances (from Lodders 2003) are included in Table 4 only because they were used in the evaluation of the B_X parameters through Equation (2) (see Jenkins 2009; Ritchey et al. 2018, 2023). They do not affect the determinations of relative ISM metallicities. Also note

³ Ritchey et al. (2023) used these STIS data, combined with archival FUSE observations, to obtain P and Cl column densities for the line of sight to HD 73882.

Table 4. Depletion Parameters for 22 Elements

Element	$\log(X/H)_\odot^a$	A_X	B_X	z_X	Reference
B	-9.15 ± 0.04	-1.471 ± 0.110	-0.801 ± 0.047	0.592	1
C	-3.54 ± 0.04	-0.101 ± 0.229	-0.193 ± 0.060	0.803	2
N	-4.10 ± 0.11	-0.000 ± 0.079	-0.109 ± 0.111	0.550	2
O	-3.24 ± 0.05	-0.284 ± 0.042	-0.153 ± 0.051	0.609	1
Mg	-4.38 ± 0.02	-0.997 ± 0.039	-0.800 ± 0.022	0.531	2
Si	-4.39 ± 0.02	-1.136 ± 0.062	-0.570 ± 0.029	0.305	2
P	-6.46 ± 0.04	-0.776 ± 0.035	-0.418 ± 0.041	0.520	3
Cl	-6.67 ± 0.06	-0.238 ± 0.046	-0.223 ± 0.061	0.593	3
Ti	-7.00 ± 0.03	-2.048 ± 0.062	-1.957 ± 0.033	0.430	2
Cr	-6.28 ± 0.05	-1.447 ± 0.064	-1.508 ± 0.055	0.470	2
Mn	-6.42 ± 0.03	-0.857 ± 0.041	-1.189 ± 0.032^b	0.520	2
Fe	-4.46 ± 0.03	-1.285 ± 0.044	-1.513 ± 0.033	0.437	2
Ni	-5.71 ± 0.03	-1.490 ± 0.062	-1.829 ± 0.035	0.599	2
Cu	-7.66 ± 0.06	-0.710 ± 0.088	-1.118 ± 0.063^b	0.711	2
Zn	-7.30 ± 0.04	-0.610 ± 0.066	-0.279 ± 0.045	0.555	2
Ga	-8.83 ± 0.06	-0.834 ± 0.064	-0.936 ± 0.062	0.607	1
Ge	-8.30 ± 0.05	-0.526 ± 0.051	-0.539 ± 0.051	0.609	1
As	-9.60 ± 0.05	-0.873 ± 0.213	-0.280 ± 0.069	0.856	1
Kr	-8.64 ± 0.08	-0.166 ± 0.059	-0.342 ± 0.081	0.663	1
Cd	-10.19 ± 0.03	-0.028 ± 0.221	-0.108 ± 0.050	0.839	1
Sn	-9.81 ± 0.04	-0.517 ± 0.070	-0.148 ± 0.044	0.691	1
Pb	-9.87 ± 0.04	-1.077 ± 0.396	-0.179 ± 0.064	0.834	1

^aSolar system abundances from [Lodders \(2003\)](#). These values are provided here because they were used in the evaluation of the B_X parameters through Equation (2). They do not affect the determinations of $[M/H]_{\text{ISM}}$.

^bThe value of B_X in this case has been adjusted to reflect the updated set of f -values adopted in the present investigation.

References—(1) [Ritchey et al. \(2018\)](#), (2) [Jenkins \(2009\)](#), (3) [Ritchey et al. \(2023\)](#).

that the values of B_{Mn} and B_{Cu} have been adjusted here to reflect the updated set of f -values adopted in the present work.

4.1. Basic Results

In Figures 1–7, we present plots of y versus x for the 84 sight lines in our final sample. Least-squares linear fits were evaluated using the Interactive Data Language (IDL) procedure FITEXY, which accounts for errors in both the x and y coordinates ([Press et al. 2007](#)). The solid black diagonal lines in Figures 1–7 represent linear fits that include all of the elemental abundance measurements available for a given sight line. The dotted black horizontal lines indicate the y -intercepts associated with these linear fits. The derived values for the slopes, which represent F_* , and the y -intercepts, which represent $[M/H]_{\text{ISM}}$, along with their associated uncer-

tainties, are presented in Table 5. In each case, we provide the reduced χ^2 value and the number of elemental abundance measurements included in the fit.

4.2. Nonlinearity in Trends of y versus x

Most of the linear fits that incorporate all of the abundance measurements available in a given direction are relatively good. The median value of χ^2/ν for the fits involving all elements is 1.10. However, the results for 12 sight lines (HD 37021, HD 37061, HD 62542, HD 73882, HD 116852, HD 121968, HD 147888, HD 147933, HD 195455, HD 198478, HD 219188, and HDE 303308) indicate relatively poor fits, with $\chi^2/\nu > 2$ (see Table 5). In some cases, a poor fit may indicate that the errors associated with the column density determinations have been underestimated. Alternatively, there could be local enhancements in the abundances

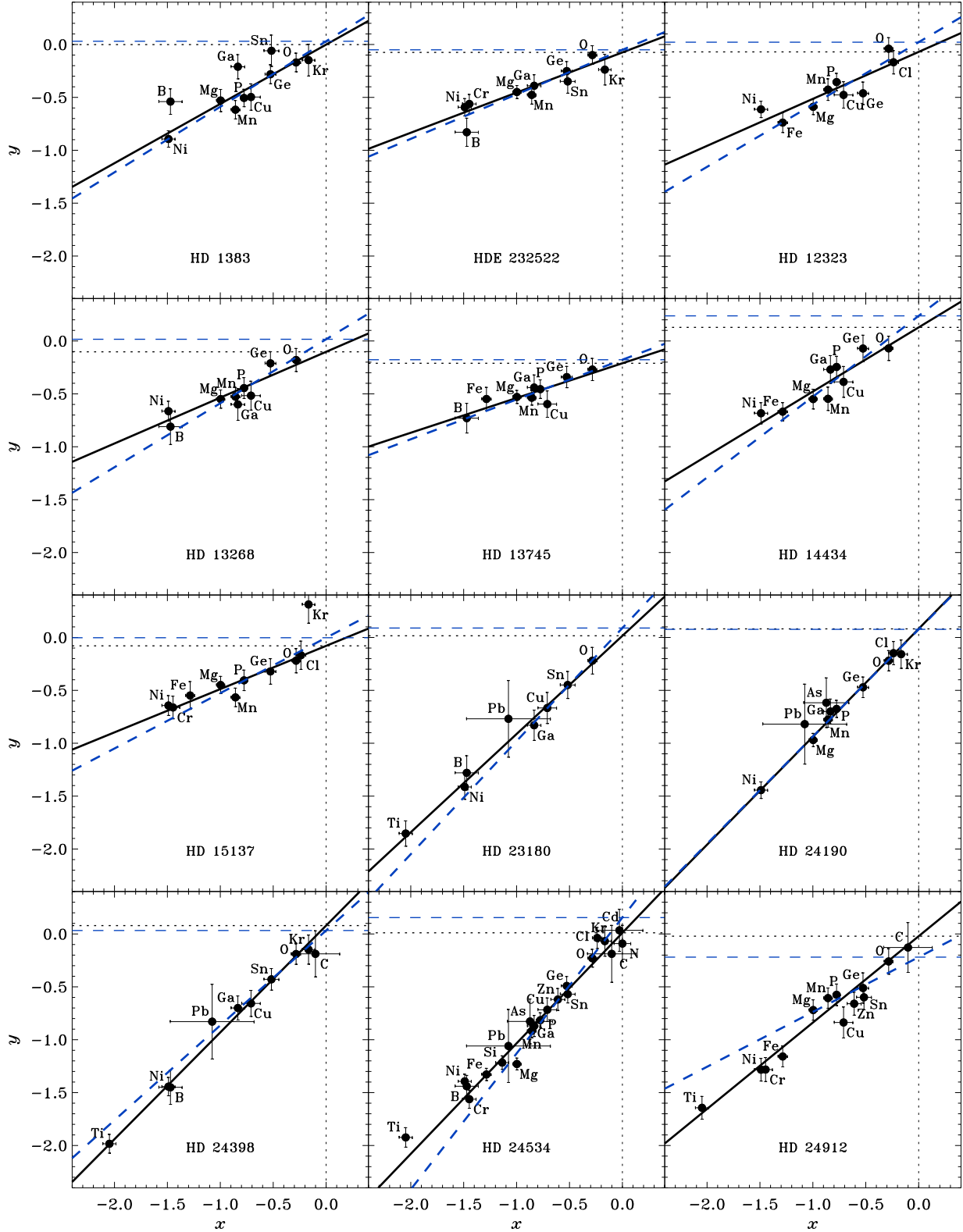


Figure 1. Derivations of relative ISM metallicities. (See Equations 9 and 10 for the definitions of y and x , respectively.) The least-squares linear fit represented by the solid black line includes measurements for all of the elements available for a given line of sight. The linear fit represented by the dashed blue line excludes the refractory elements Ti, Ni, Cr, Fe, and B. The dotted black and dashed blue horizontal lines indicate the y -intercepts associated with the linear fits represented by the solid black and dashed blue lines, respectively.

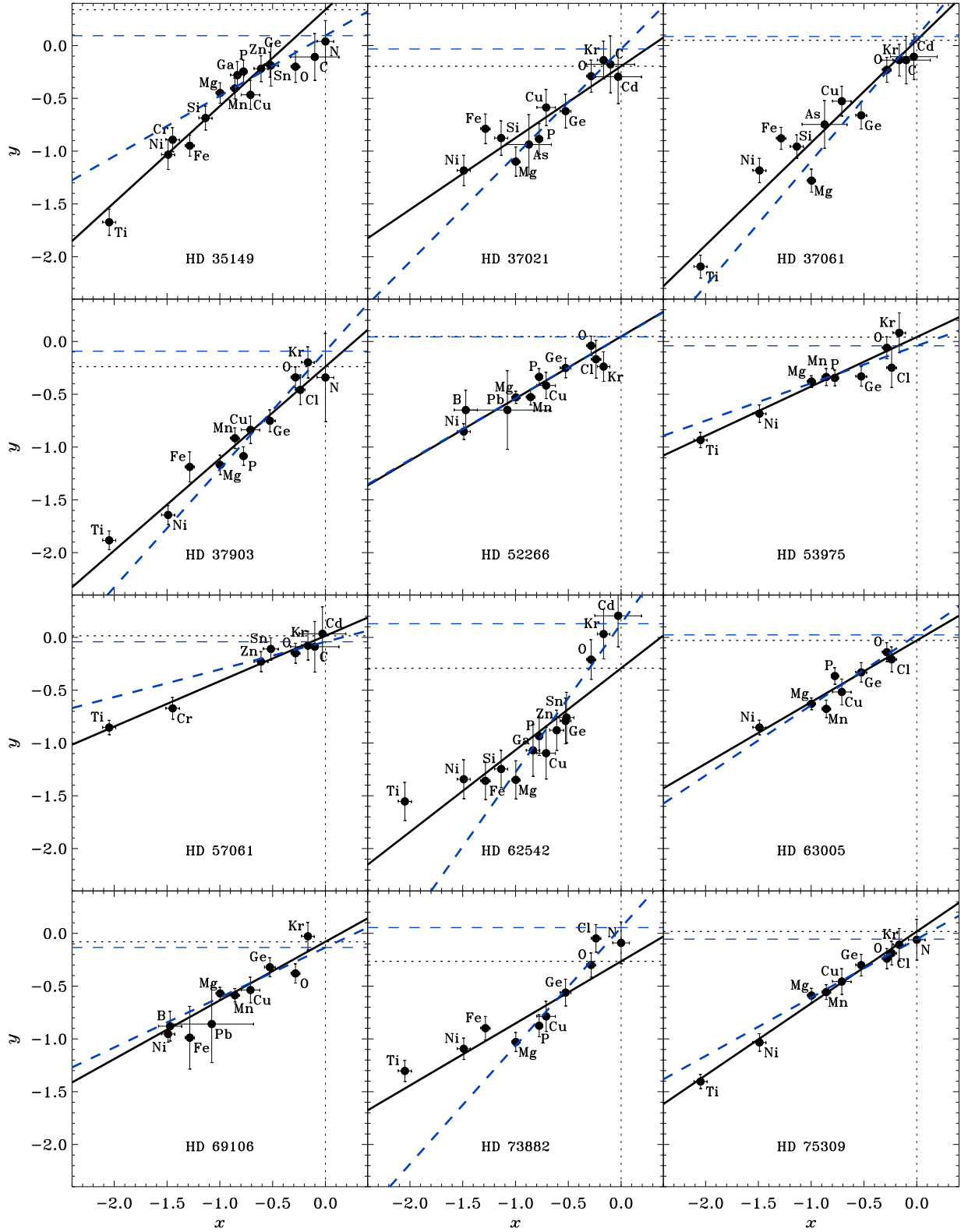


Figure 2. See caption to Figure 1.

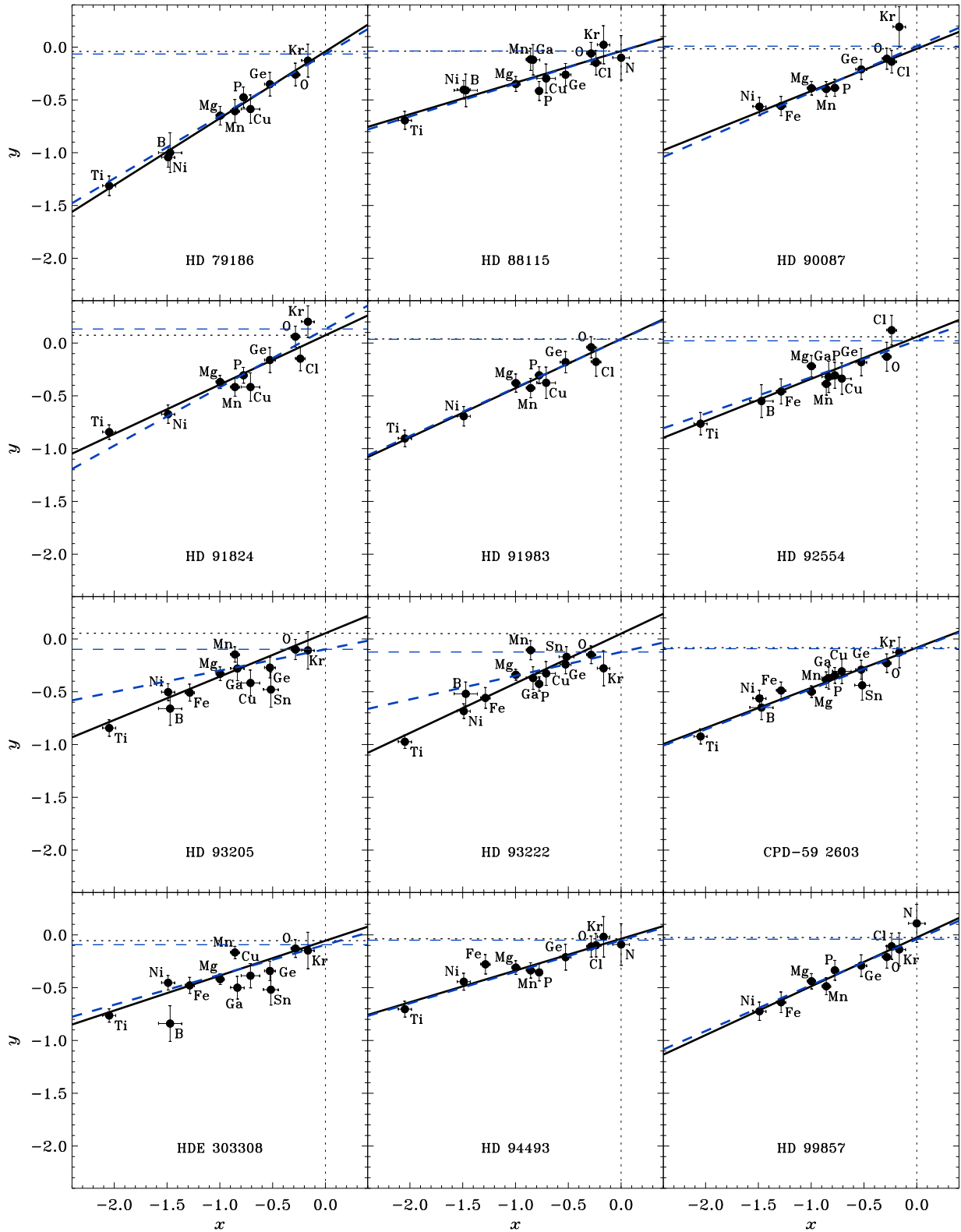


Figure 3. See caption to Figure 1.

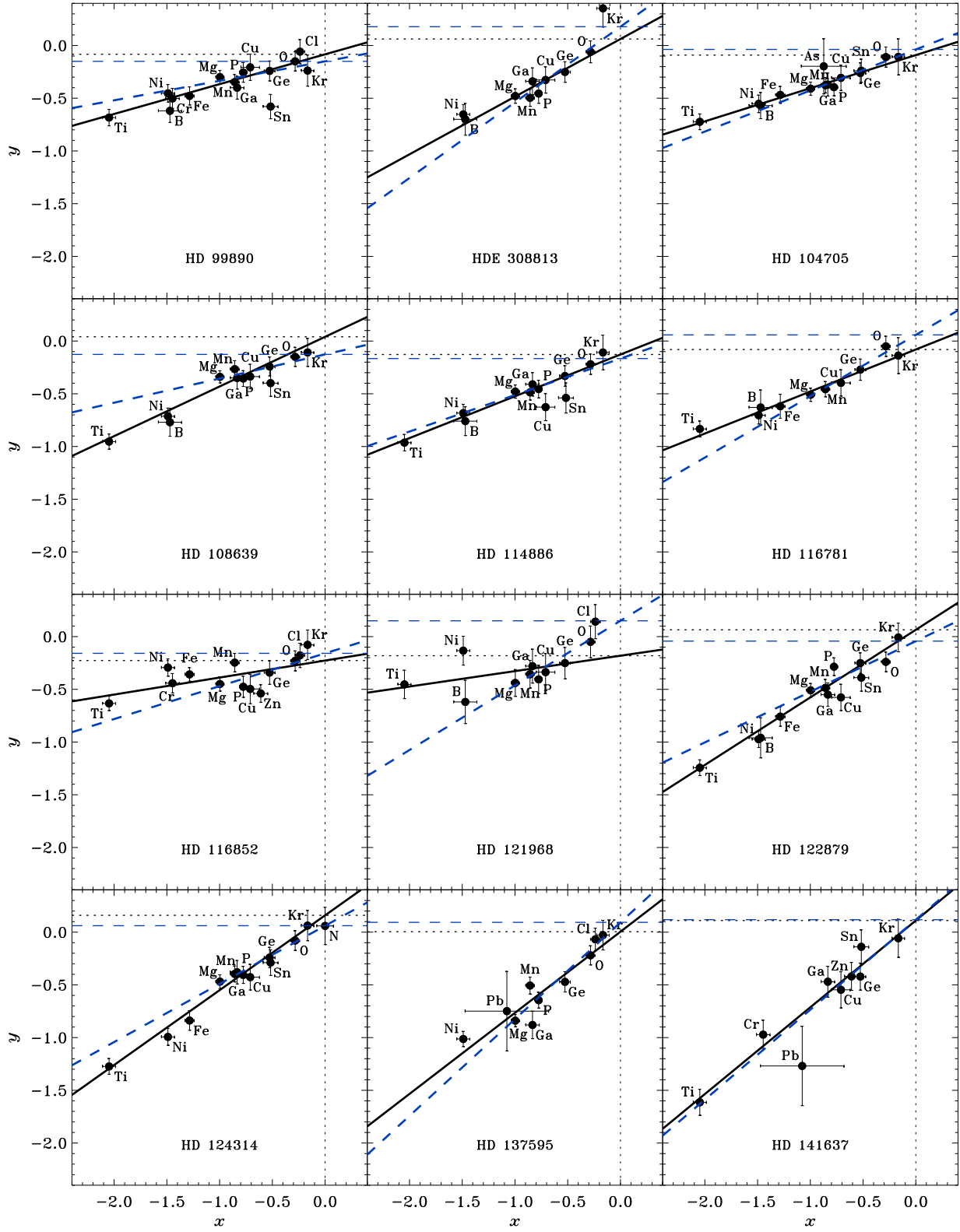


Figure 4. See caption to Figure 1.

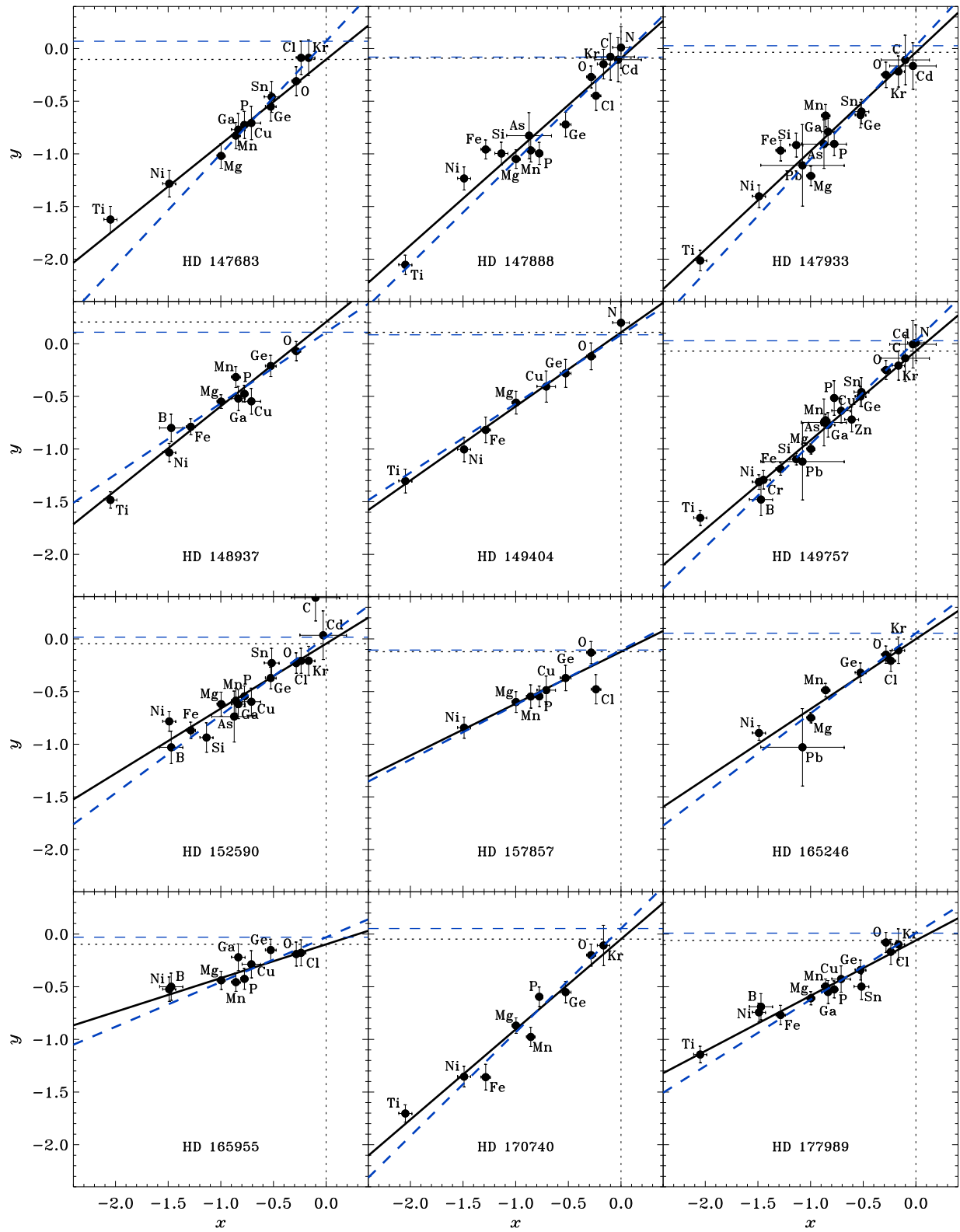


Figure 5. See caption to Figure 1.

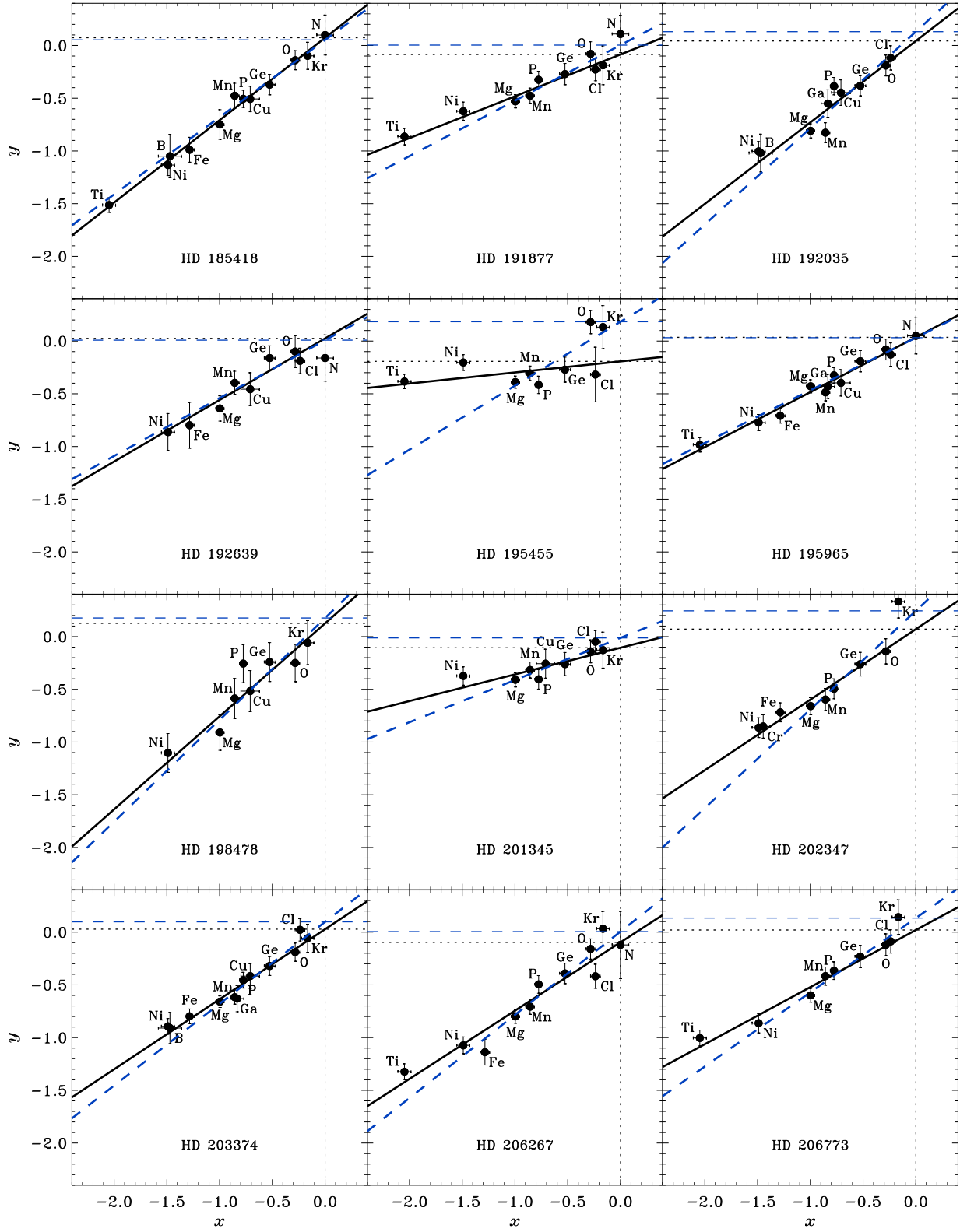


Figure 6. See caption to Figure 1.

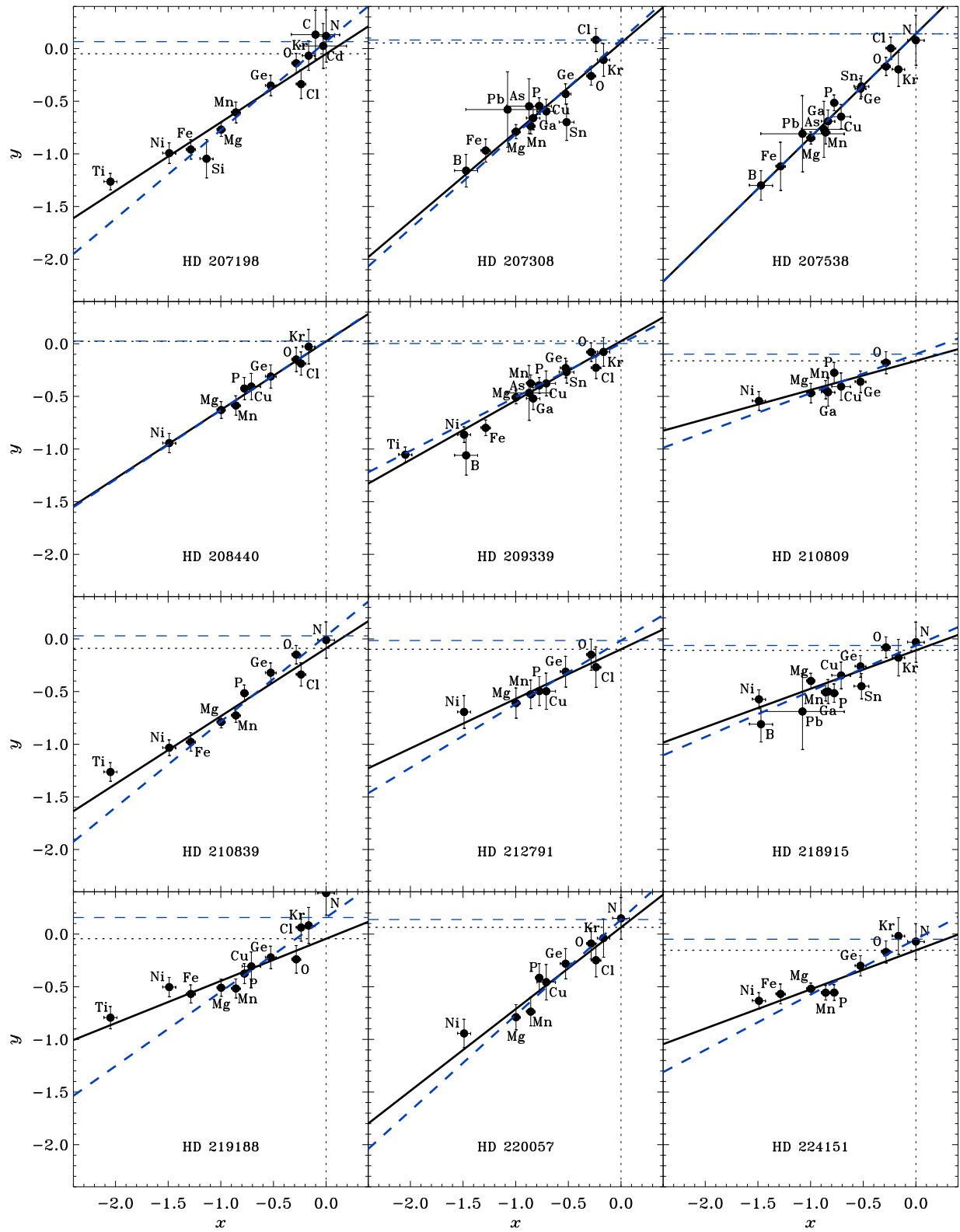


Figure 7. See caption to Figure 1.

of certain elements (and not others) due to specific nucleosynthetic processes. There could also be unusual ionization conditions in certain regions that appear to enhance the abundances of dominant ions with large ionization potentials.

For several sight lines in our sample with poor least-squares linear fits, a different explanation seems more likely. For the sight lines to HD 62542, HD 73882, HD 121968, HD 195455, and HD 219188 (for example), the y values that correspond to refractory elements (e.g., Fe, Ni, and Ti) are much larger than would be expected from an extrapolation of the trend seen for the more volatile elements. The most likely explanation for this behavior is that the stars in question probe multiple interstellar regions with very different depletion prop-

erties along the same line of sight. In this scenario, refractory elements will be heavily depleted relative to volatile ones in interstellar clouds with large values of F_* . However, these same elements will be significantly less depleted in clouds with much lower F_* values. Typically, the more depleted clouds will contain the bulk of the hydrogen along the line of sight. This effect will enhance the total sight-line column densities of refractory elements since significant portions of their gas-phase abundances originate in regions with very little total hydrogen (e.g., see [Savage et al. 1992](#); [Sembach & Savage 1996](#); [Savage & Sembach 1996](#); [Welty et al. 1999](#)).

Table 5. Relative ISM Metallicities

Star	All Elements Included				Refractory Elements Excluded			
	[M/H] _{ISM}	F_*	χ^2/ν	N^a	[M/H] _{ISM}	F_*	χ^2/ν	N^a
HD 1383	-0.001 ± 0.077	0.561 ± 0.075	1.96	11	+0.030 ± 0.100	0.619 ± 0.137	1.71	9
HD 12323	-0.070 ± 0.079	0.444 ± 0.077	1.66	9	+0.022 ± 0.096	0.589 ± 0.128	1.23	7
HD 13268	-0.102 ± 0.102	0.433 ± 0.088	0.79	9	+0.016 ± 0.126	0.605 ± 0.149	0.52	7
HD 13745	-0.211 ± 0.103	0.328 ± 0.105	0.49	9	-0.177 ± 0.113	0.376 ± 0.141	0.50	7
HD 14434	+0.129 ± 0.104	0.607 ± 0.082	1.40	9	+0.237 ± 0.136	0.764 ± 0.156	1.44	7
HD 15137	-0.079 ± 0.091	0.409 ± 0.066	1.93	10	-0.002 ± 0.099	0.524 ± 0.110	2.69	7
HD 23180	+0.016 ± 0.124	0.929 ± 0.060	0.22	8	+0.089 ± 0.211	1.069 ± 0.253	0.12	5
HD 24190	+0.081 ± 0.081	1.020 ± 0.078	0.20	11	+0.077 ± 0.088	1.013 ± 0.101	0.22	10
HD 24398	+0.079 ± 0.087	1.010 ± 0.057	0.13	10	+0.033 ± 0.129	0.897 ± 0.197	0.12	7
HD 24534	+0.011 ± 0.055	1.045 ± 0.050	1.15	22	+0.155 ± 0.068	1.285 ± 0.093	0.47	17
HD 24912	-0.021 ± 0.097	0.817 ± 0.054	1.70	13	-0.219 ± 0.117	0.518 ± 0.132	1.52	9
HD 35149	+0.339 ± 0.099	0.913 ± 0.061	1.64	16	+0.094 ± 0.110	0.571 ± 0.110	0.86	12
HD 37021	-0.196 ± 0.142	0.679 ± 0.070	4.97	12	-0.032 ± 0.149	1.009 ± 0.110	1.38	10
HD 37061	+0.050 ± 0.105	0.971 ± 0.054	6.15	12	+0.086 ± 0.119	1.181 ± 0.123	2.82	9
HD 37903	-0.238 ± 0.079	0.871 ± 0.053	1.79	12	-0.092 ± 0.095	1.118 ± 0.125	1.09	9
HD 52266	+0.047 ± 0.073	0.588 ± 0.071	0.68	11	+0.044 ± 0.082	0.582 ± 0.104	0.75	9
HD 53975	+0.042 ± 0.062	0.468 ± 0.048	0.74	9	-0.041 ± 0.083	0.355 ± 0.112	0.79	7
HD 57061	+0.015 ± 0.064	0.430 ± 0.046	0.30	8	-0.042 ± 0.102	0.262 ± 0.267	0.21	6
HD 62542	-0.292 ± 0.178	0.775 ± 0.056	5.54	14	+0.129 ± 0.192	1.406 ± 0.135	1.30	11
HD 63005	-0.029 ± 0.072	0.584 ± 0.079	1.18	8	+0.024 ± 0.086	0.666 ± 0.118	1.22	7
HD 69106	-0.080 ± 0.080	0.555 ± 0.073	0.99	10	-0.134 ± 0.086	0.473 ± 0.106	1.28	7
HD 73882	-0.265 ± 0.094	0.588 ± 0.050	5.31	10	+0.054 ± 0.108	1.120 ± 0.118	0.75	7
HD 75309	+0.017 ± 0.056	0.681 ± 0.048	0.30	10	-0.055 ± 0.070	0.553 ± 0.107	0.10	8
HD 79186	-0.041 ± 0.088	0.633 ± 0.050	0.31	10	-0.066 ± 0.107	0.589 ± 0.120	0.31	7

Table 5 continued

Table 5 (continued)

Star	All Elements Included				Refractory Elements Excluded			
	$[M/H]_{\text{ISM}}$	F_*	χ^2/ν	N^a	$[M/H]_{\text{ISM}}$	F_*	χ^2/ν	N^a
HD 88115	-0.038 ± 0.073	0.299 ± 0.042	1.33	13	-0.037 ± 0.083	0.310 ± 0.090	1.54	10
HD 90087	-0.016 ± 0.075	0.401 ± 0.068	0.65	9	$+0.009 \pm 0.081$	0.437 ± 0.099	0.77	7
HD 91824	$+0.074 \pm 0.061$	0.467 ± 0.046	1.04	10	$+0.133 \pm 0.081$	0.553 ± 0.109	1.15	8
HD 91983	$+0.039 \pm 0.072$	0.467 ± 0.048	0.41	9	$+0.035 \pm 0.101$	0.458 ± 0.130	0.52	7
HD 92554	$+0.059 \pm 0.103$	0.398 ± 0.047	1.44	11	$+0.021 \pm 0.125$	0.345 ± 0.123	2.12	8
HD 93205	$+0.054 \pm 0.069$	0.411 ± 0.045	1.84	12	-0.098 ± 0.089	0.202 ± 0.108	2.08	8
HD 93222	$+0.051 \pm 0.054$	0.471 ± 0.043	1.80	13	-0.124 ± 0.077	0.224 ± 0.103	1.73	9
HD 94493	-0.037 ± 0.064	0.300 ± 0.041	0.85	11	-0.051 ± 0.076	0.299 ± 0.093	0.47	8
HD 99857	-0.025 ± 0.078	0.462 ± 0.062	0.51	10	-0.041 ± 0.082	0.435 ± 0.091	0.65	8
HD 99890	-0.084 ± 0.064	0.283 ± 0.039	1.47	15	-0.150 ± 0.077	0.185 ± 0.088	1.95	10
HD 104705	-0.091 ± 0.066	0.314 ± 0.042	0.20	14	-0.038 ± 0.089	0.389 ± 0.105	0.20	10
HD 108639	$+0.040 \pm 0.061$	0.471 ± 0.045	1.10	12	-0.127 ± 0.080	0.229 ± 0.101	0.55	9
HD 114886	-0.128 ± 0.068	0.396 ± 0.045	0.78	12	-0.166 ± 0.089	0.346 ± 0.107	1.02	9
HD 116781	-0.080 ± 0.072	0.398 ± 0.047	0.68	10	$+0.058 \pm 0.091$	0.582 ± 0.113	0.29	6
HD 116852	-0.227 ± 0.058	0.161 ± 0.040	2.52	13	-0.158 ± 0.080	0.312 ± 0.109	2.04	9
HD 121968	-0.181 ± 0.129	0.146 ± 0.045	4.85	11	$+0.150 \pm 0.144$	0.613 ± 0.115	0.78	8
HD 122879	$+0.065 \pm 0.069$	0.641 ± 0.046	1.23	13	-0.043 ± 0.087	0.480 ± 0.105	1.38	9
HD 124314	$+0.159 \pm 0.067$	0.710 ± 0.046	0.70	13	$+0.061 \pm 0.080$	0.551 ± 0.097	0.26	10
HD 137595	$+0.004 \pm 0.074$	0.769 ± 0.077	1.86	10	$+0.093 \pm 0.084$	0.918 ± 0.105	1.36	9
HD 141637	$+0.110 \pm 0.121$	0.823 ± 0.064	0.88	9	$+0.118 \pm 0.204$	0.853 ± 0.269	0.98	7
HD 147683	-0.103 ± 0.120	0.804 ± 0.051	1.24	12	$+0.069 \pm 0.131$	1.069 ± 0.108	0.29	10
HD 147888	-0.092 ± 0.083	0.888 ± 0.048	2.92	15	-0.081 ± 0.092	0.984 ± 0.095	1.18	12
HD 147933	-0.036 ± 0.094	0.937 ± 0.052	3.31	16	$+0.026 \pm 0.111$	1.076 ± 0.111	2.46	13
HD 148937	$+0.206 \pm 0.077$	0.800 ± 0.053	1.06	11	$+0.109 \pm 0.108$	0.675 ± 0.127	1.27	7
HD 149404	$+0.108 \pm 0.114$	0.703 ± 0.050	0.31	8	$+0.085 \pm 0.123$	0.654 ± 0.113	0.19	5
HD 149757	-0.070 ± 0.055	0.847 ± 0.048	0.70	21	$+0.028 \pm 0.068$	0.981 ± 0.088	0.44	16
HD 152590	-0.045 ± 0.078	0.616 ± 0.059	0.96	17	$+0.016 \pm 0.089$	0.740 ± 0.102	0.60	14
HD 157857	-0.122 ± 0.097	0.493 ± 0.080	1.15	8	-0.106 ± 0.111	0.520 ± 0.126	1.36	7
HD 165246	-0.001 ± 0.064	0.664 ± 0.070	1.34	8	$+0.054 \pm 0.070$	0.761 ± 0.093	0.98	7
HD 165955	-0.097 ± 0.095	0.321 ± 0.083	0.87	10	-0.030 ± 0.105	0.425 ± 0.123	0.93	8
HD 170740	-0.048 ± 0.082	0.857 ± 0.061	1.92	9	$+0.053 \pm 0.109$	0.986 ± 0.146	1.99	6
HD 177989	-0.060 ± 0.066	0.525 ± 0.044	0.75	14	$+0.009 \pm 0.081$	0.631 ± 0.097	0.57	10
HD 185418	$+0.074 \pm 0.067$	0.782 ± 0.050	0.20	12	$+0.053 \pm 0.093$	0.733 ± 0.138	0.24	8
HD 191877	-0.085 ± 0.065	0.396 ± 0.045	0.88	10	$+0.003 \pm 0.076$	0.526 ± 0.092	0.67	8
HD 192035	$+0.043 \pm 0.088$	0.772 ± 0.088	1.70	10	$+0.131 \pm 0.099$	0.914 ± 0.128	1.81	8
HD 192639	$+0.025 \pm 0.112$	0.584 ± 0.109	0.68	9	$+0.008 \pm 0.111$	0.549 ± 0.143	0.91	7
HD 195455	-0.193 ± 0.061	0.105 ± 0.046	4.68	9	$+0.183 \pm 0.094$	0.606 ± 0.133	1.89	7
HD 195965	$+0.036 \pm 0.060$	0.520 ± 0.044	0.57	12	$+0.032 \pm 0.078$	0.499 ± 0.103	0.46	9
HD 198478	$+0.126 \pm 0.177$	0.882 ± 0.095	3.50	8	$+0.176 \pm 0.182$	0.965 ± 0.126	3.97	7

Table 5 continued

Table 5 (continued)

Star	All Elements Included				Refractory Elements Excluded			
	$[M/H]_{\text{ISM}}$	F_*	χ^2/ν	N^a	$[M/H]_{\text{ISM}}$	F_*	χ^2/ν	N^a
HD 201345	-0.106 ± 0.076	0.253 ± 0.075	0.99	9	-0.012 ± 0.084	0.400 ± 0.104	0.37	8
HD 202347	$+0.071 \pm 0.098$	0.669 ± 0.072	1.76	9	$+0.244 \pm 0.112$	0.935 ± 0.131	1.12	6
HD 203374	$+0.028 \pm 0.068$	0.664 ± 0.062	0.63	12	$+0.097 \pm 0.076$	0.776 ± 0.097	0.51	9
HD 206267	-0.097 ± 0.067	0.647 ± 0.047	1.85	11	$+0.005 \pm 0.079$	0.789 ± 0.099	1.51	8
HD 206773	$+0.020 \pm 0.069$	0.541 ± 0.047	1.12	9	$+0.133 \pm 0.083$	0.704 ± 0.102	0.50	7
HD 207198	-0.050 ± 0.067	0.650 ± 0.048	1.11	13	$+0.066 \pm 0.076$	0.840 ± 0.094	0.49	10
HD 207308	$+0.053 \pm 0.083$	0.847 ± 0.089	0.91	14	$+0.081 \pm 0.088$	0.896 ± 0.112	1.02	12
HD 207538	$+0.140 \pm 0.080$	0.980 ± 0.090	0.43	15	$+0.139 \pm 0.079$	0.980 ± 0.101	0.50	13
HD 208440	$+0.022 \pm 0.082$	0.651 ± 0.083	0.18	9	$+0.025 \pm 0.091$	0.657 ± 0.118	0.21	8
HD 209339	$+0.025 \pm 0.059$	0.564 ± 0.043	0.75	15	$+0.002 \pm 0.075$	0.509 ± 0.094	0.40	11
HD 210809	-0.163 ± 0.095	0.276 ± 0.084	0.63	8	-0.099 ± 0.123	0.371 ± 0.145	0.62	7
HD 210839	-0.090 ± 0.064	0.644 ± 0.051	1.58	10	$+0.029 \pm 0.074$	0.815 ± 0.098	1.19	7
HD 212791	-0.098 ± 0.143	0.471 ± 0.098	0.52	8	-0.015 ± 0.151	0.604 ± 0.137	0.19	7
HD 218915	-0.108 ± 0.083	0.365 ± 0.070	1.55	13	-0.063 ± 0.091	0.435 ± 0.103	1.58	11
HD 219188	-0.044 ± 0.083	0.401 ± 0.049	2.26	12	$+0.157 \pm 0.095$	0.705 ± 0.103	0.94	9
HD 220057	$+0.064 \pm 0.124$	0.776 ± 0.080	1.47	10	$+0.138 \pm 0.128$	0.908 ± 0.104	1.02	9
HD 224151	-0.154 ± 0.071	0.372 ± 0.072	1.35	9	-0.049 ± 0.079	0.526 ± 0.109	1.06	7
HDE 232522	-0.075 ± 0.073	0.380 ± 0.065	0.78	10	-0.050 ± 0.083	0.421 ± 0.109	0.59	7
HDE 303308	-0.055 ± 0.055	0.331 ± 0.043	2.63	12	-0.093 ± 0.080	0.284 ± 0.110	3.45	8
HDE 308813	$+0.062 \pm 0.089$	0.547 ± 0.085	1.23	10	$+0.178 \pm 0.104$	0.717 ± 0.132	1.06	8
CPD-59 2603	-0.083 ± 0.060	0.380 ± 0.043	0.62	13	-0.092 ± 0.079	0.382 ± 0.100	0.42	9

^aNumber of elemental abundance measurements included in the least-squares linear fit.

A detailed abundance analysis by Welty et al. (2020) confirms this scenario for HD 62542. Those authors derived abundances for a variety of different atomic and molecular species and reported total column densities for two separate groups of components along the line of sight. The main component near $v_{\text{LSR}} = -5 \text{ km s}^{-1}$ is heavily depleted and is estimated to contain nearly 90% of the total hydrogen column density. All of the other velocity components along the line of sight, which constitute very little in terms of total hydrogen, show much less depletion of refractory elements (e.g., see Figure 6 in Welty et al. 2020). If we had knowledge of the amount of hydrogen contained in individual velocity components along lines of sight showing nonlinear trends in y versus x , then we could conceivably derive values of $[M/H]_{\text{ISM}}$ for each component. Welty et al. (2020) obtained estimates for the amount of hydrogen present in the two groups of components observed toward HD 62542 based, in part, on empirical correlations

between $N(\text{H I})$, $N(\text{H}_2)$, $N(\text{H}_{\text{tot}})$ and the abundances of other interstellar constituents (e.g., CH, Na I, and the diffuse interstellar band at 5780 Å). The issue with using a similar approach in the present investigation is that such correlations rely on implicit assumptions about the metallicities in the clouds under consideration. If the metallicity in a given parcel of gas is significantly different from the typical ISM metallicity, then the usual correlations would (presumably) no longer apply.

A simple solution to the problem of nonlinearity in trends of y versus x is to perform a second set of least-squares linear fits in which the refractory elements are excluded. In Figures 1–7, the dashed blue diagonal lines represent linear fits that exclude the elements Ti, Ni, Cr, Fe, and B (all of which have $A_X < -1.2$). The dashed blue horizontal lines indicate the y -intercepts associated with these restricted fits. The resulting values of $[M/H]_{\text{ISM}}$ and F_* are again provided in Table 5. With this revised set of linear fits, the median value of χ^2/ν is now 0.92 and there are fewer cases where the reduced

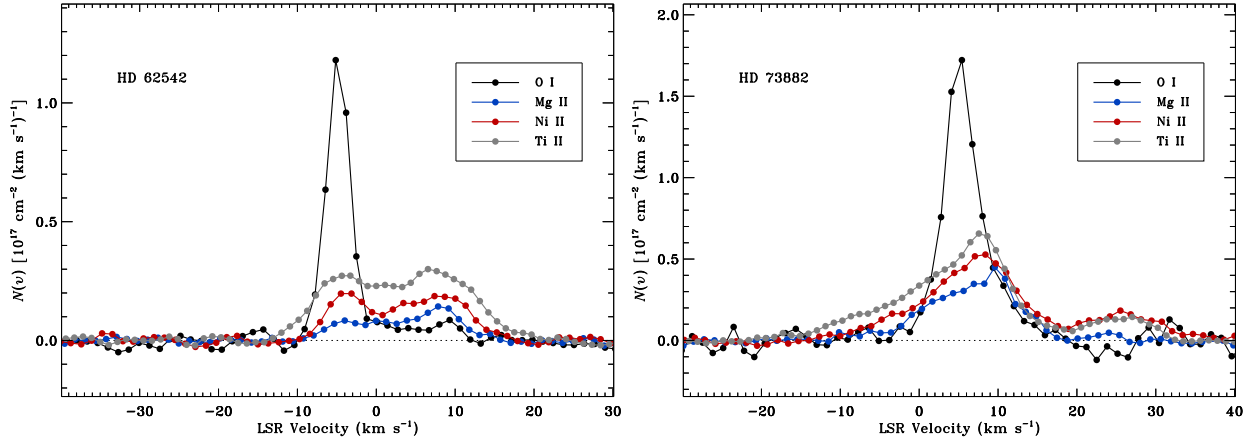


Figure 8. Apparent column density profiles of O I, Mg II, Ni II, and Ti II toward HD 62542 (left panel) and HD 73882 (right panel) from HST/STIS observations of the O I λ 1355, Mg II λ 1239, and Ni II λ 1317 lines and VLT/UVES observations of the Ti II λ 3383 line. The column density scale applies to the O I profile. Profiles for the other species have been scaled to account for differences in the cosmic abundances of the elements and to adjust for the expected differences in the depletions of the elements at a particular value of F_* . The adopted values of F_* (0.775 for HD 62542; 0.588 for HD 73882) correspond to the values obtained from our linear fits that include all of the available elements.

χ^2 values are significantly larger than 2. However, the typical uncertainties in the derived values of $[M/H]_{\text{ISM}}$ and F_* are larger for these fits than for the original linear fits (because there are fewer elements considered and the elements that are included in the fits span a smaller range in A_X).

If we compare for a given line of sight the linear fit that includes all available elements to the linear fit restricted to non-refractory elements, we find that, in general, the restricted fits result in steeper slopes (i.e., larger sight-line depletion factors) and higher relative ISM metallicities. In most cases, the differences in the outcomes for $[M/H]_{\text{ISM}}$ and F_* between the two fits are small and within the uncertainties. Nevertheless, there does appear to be a systematic shift toward steeper slopes when the refractory elements are excluded. This indicates that the issue discussed above, where a line of sight samples multiple distinct gas regions with different depletion properties, is fairly common, although in most cases the effect appears to be rather minor.

There are four sight lines where the difference in slope between the linear fits with and without the refractory elements is larger than three times the associated uncertainty and these sight lines have been mentioned before: HD 62542, HD 73882, HD 121968, and HD 195455. Both HD 62542 and HD 73882 are well-known examples of translucent sight lines (e.g., Snow et al. 2000; Rachford et al. 2002; Sonnentrucker et al. 2007; Welty et al. 2020). The dominant velocity components in these directions show heavy depletions. (Our fits that exclude refractory elements indicate that $F_* > 1$ in both cases.) However, both sight lines also show additional velocity components where the gas-phase abundances of

refractory elements are enhanced (see Figure 8). The other two sight lines showing large discrepancies in the derived slope parameters are different. Both HD 121968 and HD 195455 are located at high Galactic latitude. (HD 121968 is the star that has the largest z distance in Table 1.) These two sight lines appear to probe a combination of disk gas with moderate depletions and halo gas with very low depletions. In all four cases, however, it is the sampling of multiple distinct gas regions with different depletion properties that gives rise to the nonlinear trends in plots of y versus x .

In Figure 8, we provide a demonstration of the extreme differences in the velocity distributions of volatile and refractory species toward HD 62542 and HD 73882. In this figure, we plot the apparent column densities of O I, Mg II, Ni II, and Ti II as a function of velocity. The Mg II, Ni II, and Ti II profiles have been scaled to that of O I, accounting for differences in the cosmic abundances of the elements (Table 4) and adjusting for the expected differences in the depletions of the elements at a particular value of F_* . The adopted values of F_* (0.775 for HD 62542; 0.588 for HD 73882) correspond to the values obtained from our linear fits that include all of the available elements in these directions.

Clearly, there are significant differences in the depletion properties of the various gas components seen toward HD 62542 and HD 73882. At the velocity of the dominant absorption component in each direction, the apparent column density profile of O I is greatly enhanced compared to those of the more refractory species. This indicates that a much larger value of F_* is needed to characterize the absorption. Indeed, Welty et al. (2020) find a value of $F_* \approx 1.5$ for the main component toward

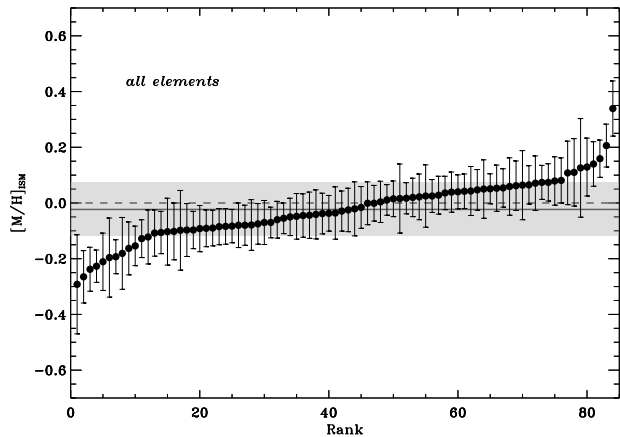


Figure 9. Relative ISM metallicities determined for a sample of 84 sight lines with abundance measurements for at least eight different elements. These metallicities correspond to the linear fits that include all elements for a given line of sight. The solid dark gray horizontal line indicates the weighted mean metallicity of the sample (-0.023 ± 0.008), while the light gray shaded region indicates the ($\pm 1\sigma$) weighted standard deviation (0.096 dex). The dashed horizontal line marks the location of $[M/H]_{\text{ISM}} = 0.0$.

HD 62542. This is similar to the value we obtain for this sight line ($F_* \approx 1.4$) from our linear fit that excludes the most refractory elements.

The velocity distributions of the more refractory species toward HD 62542 and HD 73882 are much broader (and show additional peaks) compared to the relatively narrow O I profiles. The enhanced column densities of refractory elements indicate that much lower values of F_* are required for these additional components. (Welty et al. (2020) find that a value of $F_* \approx 0.3$ characterizes the “other” components toward HD 62542.) However, the gas-phase abundances of Ni II and Ti II are enhanced (relative to Mg II) even at the velocities of the dominant absorption components toward HD 62542 and HD 73882. No single value of F_* can simultaneously account for the observed column densities of O I, Mg II, Ni II, and Ti II in these strongly-depleted components. This could indicate that the depletion strength increases with depth into the cloud and/or that the different species have different volume distributions at a given velocity. Regardless, the above demonstration shows that the problem of nonlinearity in plots of y versus x can sometimes apply to individual velocity components, and not just to lines of sight as a whole.

4.3. Metallicity Distributions

The main objective of our investigation is to examine for a large representative sample the distribution of metallicities seen along sight lines probing the local

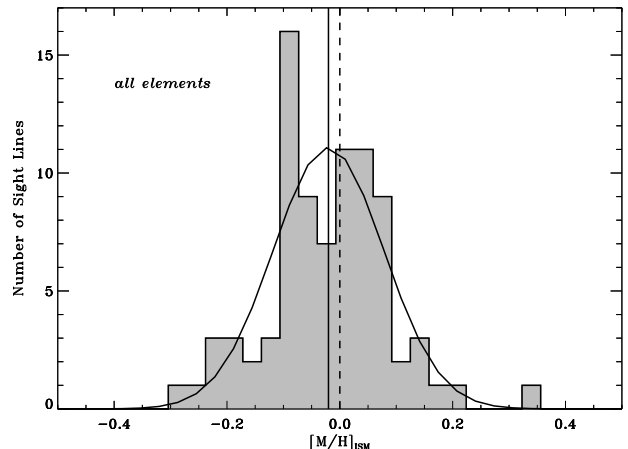


Figure 10. Distribution of relative ISM metallicities. These metallicities correspond to the linear fits that include all elements for a given line of sight. A Gaussian function is fitted to the observed distribution, which is represented by a histogram. The solid vertical line indicates the mean value from the Gaussian fit (-0.020). The standard deviation from the fit is 0.098 dex. The dashed vertical line marks the location of $[M/H]_{\text{ISM}} = 0.0$.

Galactic ISM. While the method we employ is incapable of providing us with the metallicity of the ISM relative to an adopted solar (or cosmic) abundance standard, it can tell us the degree to which the metallicity varies from one sight line to another. In Figure 9, the relative ISM metallicities for the 84 sight lines in our final sample are plotted according to their rank. These are the metallicities derived from the least-squares linear fits that include all elemental abundance measurements available for a given line of sight. The weighted mean value of $[M/H]_{\text{ISM}}$ for this set of measurements is -0.023 ± 0.008 . (For this calculation, we have adopted weights that correspond to the inverse squares of the measurement uncertainties.) Since the metallicities being derived are measured relative to the average ISM metallicity (Section 2), one would expect this mean value to be close to zero. (It need not be exactly zero, of course, since the sample of stars examined in the present survey differs from those originally used to derive the element coefficients; Jenkins 2009; Ritchey et al. 2018, 2023). Still, the mean value given above is consistent with zero at only the 3σ level. The reason for this discrepancy may be that the linear fits that include all elements tend to underestimate the slope of the trend of y versus x because the refractory elements have slightly enhanced gas-phase abundances relative to volatiles when the sight line probes multiple distinct regions with different depletion properties.

A statistic more important than the mean value in this context is the standard deviation, which should in-

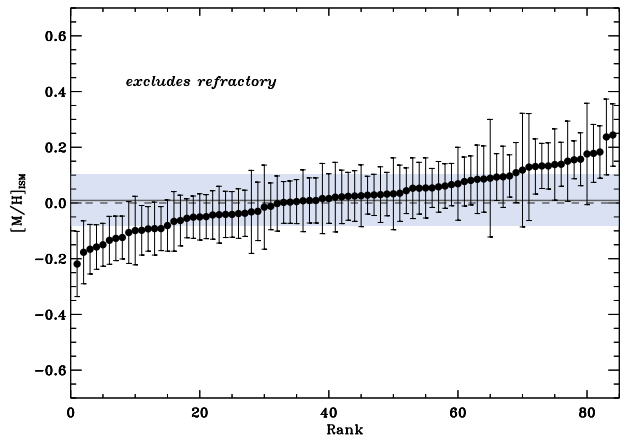


Figure 11. Same as Figure 9 except that the metallicities correspond to the linear fits that exclude the refractory elements Ti, Ni, Cr, Fe, and B. The weighted mean value of $[M/H]_{\text{ISM}}$ in this case is $+0.009 \pm 0.010$, while the weighted standard deviation is 0.093 dex.

dicating the degree of chemical homogeneity exhibited by the interstellar gas in the solar neighborhood. For the linear fits that include all of the available elements, the weighted standard deviation in $[M/H]_{\text{ISM}}$ is 0.096 dex. This may be compared to the median of the uncertainties in $[M/H]_{\text{ISM}}$, which is 0.078 dex. To test whether the measured dispersion in $[M/H]_{\text{ISM}}$ is significant, we can calculate a χ^2 value for the sample:

$$\chi^2 = \sum_{i=1}^N \frac{([M/H]_{\text{ISM},i} - \langle [M/H]_{\text{ISM}} \rangle)^2}{\sigma([M/H]_{\text{ISM},i})^2}, \quad (15)$$

where $[M/H]_{\text{ISM},i}$ is the metallicity for the i th sight line, $\sigma([M/H]_{\text{ISM},i})$ is the uncertainty in that measurement, $\langle [M/H]_{\text{ISM}} \rangle$ is the weighted mean value derived above, and N is the number of measurements. For the linear fits that include all of the available abundance measurements, the χ^2 value, divided by the number of degrees of freedom, is $132.1/83 = 1.59$. Under the proposition that all sight lines have the same value of $[M/H]_{\text{ISM}}$, the probability of obtaining a χ^2 statistic worse than this is 0.000495. Evidently, there is a small amount of scatter that is unaccounted for by the observational uncertainties (or the observational uncertainties have been underestimated). In Figure 10, we plot the metallicity distribution derived from the unrestricted linear fits. A Gaussian function is fitted to the observed distribution. The mean and standard deviation derived from the Gaussian fit are both nearly equal to the values obtained directly from the sample. However, the distribution appears to be somewhat irregular. In particular, there is a pileup in the number of sight lines with metallicities that are ~ 0.09 dex below average.

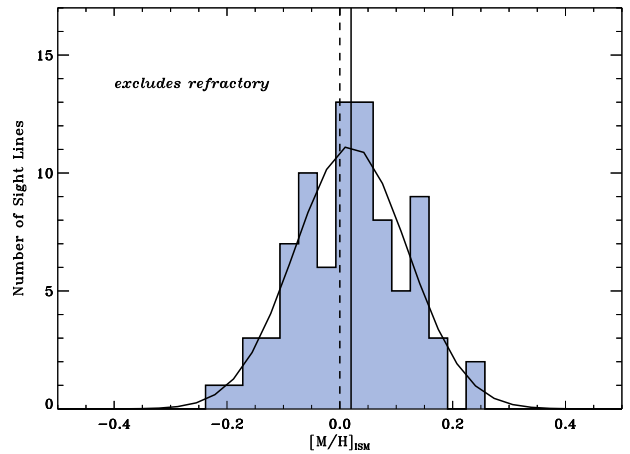


Figure 12. Same as Figure 10 except that the metallicities correspond to the linear fits that exclude the refractory elements Ti, Ni, Cr, Fe, and B. The mean value from the Gaussian fit in this case is $+0.020$, while the standard deviation is 0.100 dex.

The excess scatter in the values of $[M/H]_{\text{ISM}}$ obtained from the unrestricted linear fits seems to arise from the varying degrees of nonlinearity observed in the trends of y versus x displayed in Figures 1–7. Ultimately, the cause of this variation is the extent to which different sight lines are contaminated by gas regions with depletion properties that are distinctly different from that which characterizes the bulk of the interstellar material along the line of sight. As an example, consider a sight line that probes a typical heavily-depleted diffuse molecular cloud but is contaminated by unrelated gas regions exhibiting much lower depletion strengths. In this case, the total gas-phase abundances of refractory elements will be enhanced relative to volatiles, and a linear fit that includes all elements will underpredict the slope and y -intercept that pertain to the dominant interstellar cloud. For a sight line such as that described here, a fit that excludes the refractory elements will provide a more accurate representation of the depletion strength and the relative ISM metallicity. (Extreme examples of this phenomenon are provided by the sight lines to HD 62542 and HD 73882; see Figures 2 and 8.)

In Figure 11, we provide a plot analogous to Figure 9 showing the relative ISM metallicities derived from the linear fits that exclude the elements Ti, Ni, Cr, Fe, and B. The weighted mean value of $[M/H]_{\text{ISM}}$ for this set of measurements is $+0.009 \pm 0.010$, while the weighted standard deviation is 0.093 dex. The mean value, therefore, is now statistically indistinguishable from zero and the standard deviation is somewhat smaller compared to the previous set of results. As stated earlier, the typical uncertainty in the derivations of $[M/H]_{\text{ISM}}$ is larger for the fits restricted to non-refractory elements. Con-

sequently, the median of the uncertainty values (0.091 dex) is now almost identical to the weighted standard deviation (0.093 dex). From Equation (15), we find that the χ^2/ν value for this set of measurements is $83.9/83 = 1.01$, indicating that there is essentially no measured variation in $[M/H]_{\text{ISM}}$ beyond that which is expected from the observational uncertainties. (The probability of obtaining a worse value for the χ^2 statistic in this case is 0.451.) The analog of Figure 10 for the metallicities derived from the restricted linear fits is shown in Figure 12. As in the previous case, the mean and standard deviation of a Gaussian function fitted to the observed distribution are consistent with the values determined directly from the sample. However, the distribution of $[M/H]_{\text{ISM}}$ values for this set of results is now noticeably more regular.

Regardless of which set of derivations of $[M/H]_{\text{ISM}}$ is considered, our results provide strong evidence for the chemical homogeneity of the interstellar gas in the solar neighborhood. Any metallicity variations present must be smaller than the typical measurement uncertainties. These results stand in sharp contrast to those presented by De Cia et al. (2021). Importantly, we see no evidence for very low metallicity gas (such as that reported in De Cia et al. 2021) along any of the 84 sight lines in our sample. A detailed comparison between the metallicity derivations presented in this work and those of De Cia et al. (2021) is provided in Section 5.1.

5. DISCUSSION

The most significant result of our analysis of relative ISM metallicities is that the spread in metallicities exhibited by the sight lines in our sample is small and only slightly larger than the typical measurement uncertainties. Most of the column density measurements used in our metallicity analysis were derived from moderate strength atomic transitions (e.g., O I $\lambda 1355$, Mg II $\lambda\lambda 1239, 1240$, P II $\lambda 1532$, Ti II $\lambda 3383$, Mn II $\lambda\lambda 1197, 1201$, Ni II $\lambda 1317$, Cu II $\lambda 1358$, Ge II $\lambda 1237$, and Kr I $\lambda 1235$) recorded at high spectral resolution ($\Delta v \sim 2\text{--}4 \text{ km s}^{-1}$). It is relatively straightforward to extract accurate column densities from such data using either the AOD or profile fitting method.⁴ Furthermore, our sample is both large enough to be statistically significant and diverse enough to be representative of the

⁴ A small fraction ($\sim 11\%$) of the measurements used in our analysis were derived from low-resolution FUSE observations. However, in these cases, the column densities are adequately constrained through the use of curves of growth that include very weak transitions (e.g., Jensen et al. 2007; Jensen & Snow 2007) or through Voigt profile fitting of weak lines, adopting component structures from higher resolution data (e.g., Ritchey et al. 2023).

local Galactic ISM. The inclusion of a wide variety of elements that exhibit a range of different depletion behaviors ensures that our linear fits are well constrained (even when the more refractory elements are excluded). It is also important to note that the elements considered in our investigation are produced through a variety of different nucleosynthetic processes. (For example, we have representatives of α -process elements, Fe-group elements, neutron-capture elements, and elements produced through cosmic ray spallation.) This helps to ensure that we are probing variations in the overall metallicity and are not overly influenced by any potential variations in one process or another.

5.1. Comparison with the Results of De Cia et al.

De Cia et al. (2021) reported relative ISM metallicities for a sample of 25 sight lines probing the solar neighborhood out to a distance of 3 kpc. Most of their column density measurements were made using newly-acquired medium-resolution (E230M) STIS spectra. (STIS E230M spectra have a velocity resolution of $\sim 10 \text{ km s}^{-1}$.) De Cia et al. (2021) derive metallicity estimates for their sight lines using two approaches. The one that they term the “ F_* method” is the same as that adopted in this investigation (see Section 2). Thus, a direct comparison of results is possible for any sight lines in common between our investigation and theirs.⁵

There are eight sight lines in common between our metallicity study and that of De Cia et al. (2021): HD 23180 (*o* Per), HD 24534 (X Per), HD 62542, HD 73882, HD 147933 (ρ Oph A), HD 149404, HD 206267, and HD 207198. In every case, our value for the relative ISM metallicity is substantially larger than the value given by De Cia et al. (2021). (The differences range from 0.2 to 0.8 dex.) The largest discrepancies are found for the sight lines to X Per, HD 62542, and HD 73882, ρ Oph A, and HD 207198. These are among the sight lines with the lowest reported metallicities in De Cia et al. (2021) and many of these sight lines show nonlinear trends in plots of y versus x . De Cia et al. (2021) underestimate the metallicities in these directions primarily because they derive their estimates from only the most refractory elements, and these elements tend to exhibit shallower slopes (in the x - y plane) compared to the more volatile elements.

The most thorough comparison between our investigation and that of De Cia et al. (2021) can be made for the

⁵ It is important to understand that the metallicities derived by De Cia et al. (2021) using the “ F_* method” are *relative* ISM metallicities, just as they are in this investigation. They are not metallicities relative to an adopted solar abundance standard as is claimed in De Cia et al. (2021).

line of sight to X Per. For this sight line, we have column density measurements for all 22 elements considered in our metallicity analysis. The uncertainties in the derived values of $[M/H]_{\text{ISM}}$ and F_* are thus among the smallest for this direction. De Cia et al. (2021) find a depletion-corrected metallicity of $[M/H] = -0.57 \pm 0.12$ and a sight-line depletion factor of $F_* = 0.61 \pm 0.09$ toward X Per. However, their least-squares linear fit includes only Ti, Cr, Fe, Ni, and Zn. Abundance results for C, N, and O are plotted in the panel showing their linear fit for X Per (see Extended Data Fig. 3 in De Cia et al. 2021) but these elements are not included in the fit. The y values for these volatile elements are clearly displaced upward relative to the fitted line that corresponds to the more refractory elements. Thus, if the volatile elements had been included in the fit, the slope of the fitted line would be steeper and the y -intercept (i.e., the metallicity) would be much larger.

From our least-squares linear fit that includes all 22 elements measured toward X Per, we find $[M/H]_{\text{ISM}} = +0.011 \pm 0.055$ and $F_* = 1.045 \pm 0.050$ (Figure 1; Table 5). Thus, the metallicity is indistinguishable from the average ISM metallicity, and the sight-line depletion factor is approximately equal to one, as would be expected for X Per, which is a well-known translucent sight line. When the refractory elements are excluded from the fit, we find $[M/H]_{\text{ISM}} = +0.155 \pm 0.068$ and $F_* = 1.285 \pm 0.093$. Thus, this appears to be another case where the dominant interstellar cloud along the line of sight shows heavy depletions, but there are additional components where the gas-phase abundances of refractory elements are enhanced. (The slope parameters obtained from the two different linear fits for X Per differ at only the 2σ level, however.)

Regardless of which of our linear fits one considers to be the most appropriate, our result for the relative ISM metallicity toward X Per is considerably larger than that obtained by De Cia et al. (2021). There are two main reasons for this discrepancy. First, as already mentioned, the volatile elements (C, N, and O) are excluded from the De Cia et al. (2021) analysis. Second, the Zn II column density reported by De Cia et al. (2021) underestimates the true column density by ~ 0.35 dex. De Cia et al. (2021) report a value of $\log N(\text{Zn II}) = 13.13 \pm 0.04$, which they obtain by integrating the AOD profiles of the Zn II $\lambda 2026$ and $\lambda 2062$ lines seen in medium-resolution STIS echelle spectra.⁶ Our result

⁶ The value quoted here for $\log N(\text{Zn II})$ from De Cia et al. (2021) includes an adjustment of $+0.10$ dex to account for the difference in the adopted f -values of the Zn II lines between our investigation and theirs. However, as mentioned in Section 3.1,

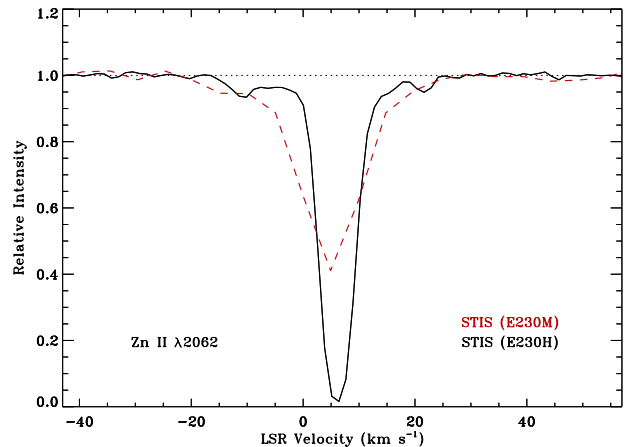


Figure 13. Comparison between high-resolution (E230H) and medium-resolution (E230M) STIS spectra covering the Zn II $\lambda 2062$ transition toward X Per. The Zn II absorption line is heavily saturated in this direction despite the appearance of the line in the E230M spectrum.

of $\log N(\text{Zn II}) = 13.48 \pm 0.07$ is derived from high-resolution (E230H) STIS observations of the Zn II $\lambda 2062$ line (the weaker member of the Zn II doublet) using a Voigt profile fitting technique. In this fit, the component structure of the relatively strong Zn II $\lambda 2062$ line is constrained by the results for other dominant ions with more moderate strength transitions (for more details see A. M. Ritchey, in preparation).

The danger of extracting column densities from relatively strong interstellar absorption lines observed at moderate resolution using the AOD method is illustrated in Figure 13. In this figure, we compare the appearance of the Zn II $\lambda 2062$ line toward X Per in medium-resolution and high-resolution STIS echelle spectra. The E230H spectrum clearly shows that the Zn II line is heavily saturated despite the fact that, in the E230M spectrum, the line has a “pointed” appearance and the relative intensity at line center is far from zero. A straight integration of the line gives $\log N(\text{Zn II}) = 13.17$ for the E230H spectrum and 12.91 for E230M, while the integrated equivalent widths are nearly the same (58.5 and 58.9 mÅ, respectively). De Cia et al. (2021) apply a correction to their integrated Zn II column densities, based on the prescription of Jenkins (1996), arriving at a value of 13.13 for X Per. However, it appears that the optical depth correction is inadequate in this case since the integrated value from the E230H spectrum (13.17) represents a lower limit to the true column density.

the difference in the f -values does not affect the outcome for $[M/H]_{\text{ISM}}$.

The Zn II column densities measured by De Cia et al. (2021) have a significant impact on their determinations of metallicities since Zn represents one of the endpoints of their linear fits (the other endpoint being Ti). If many of their Zn II column densities are underestimated, as demonstrated here for X Per, then their metallicities are also underestimated. Indeed, by comparing the predicted values of y for Zn (based on our linear fits) to the values reported by De Cia et al. (2021) for the sight lines in common, we find that De Cia et al. (2021) appear to have underestimated the Zn II column densities by 0.1 to 0.6 dex depending on the sight line. The larger issue with the De Cia et al. (2021) analysis, however, is that their linear fits do not include any of the relatively undepleted elements (such as C, N, O and Kr) despite the fact that measurements for these elements are readily available for many of their sight lines. Most of the volatile element measurements (shown in Extended Data Fig. 3 in De Cia et al. 2021) are displaced upward relative to the fitted lines that correspond to the more refractory elements. Had these volatile elements been included in their fits, the slopes would generally be steeper and the derived metallicities would be higher.

De Cia et al. (2021) address the discrepancy in their results between the volatile elements and the refractory ones. The same nonlinearity in plots of y versus x is seen for many of the sight lines in our investigation (Section 4.2). However, De Cia et al. (2021) attribute the discrepancy to a mixture of solar metallicity gas and very low metallicity (pristine) gas along the same line of sight.⁷ The problem with this interpretation is that it is purely speculative. Let us consider once again the situation where a line of sight passes through a diffuse molecular cloud characterized by heavy depletions but also samples gas regions with much lower depletion strengths. According to our interpretation, the heavily depleted cloud contains the bulk of the hydrogen along the line of sight. The other components constitute very little in terms of total hydrogen yet much of the gas-phase abundances of refractory elements are contained in those minor components. De Cia et al. (2021) would argue that those gas regions with lower depletion strengths also have much lower metallicities. However, there is no evidence to support this assertion. The problem is that we are unable to directly determine what fraction of the total hydrogen column density is associated with each of the various line-of-sight components. The De Cia et al. (2021) interpretation implies that a large fraction of the total hydrogen column den-

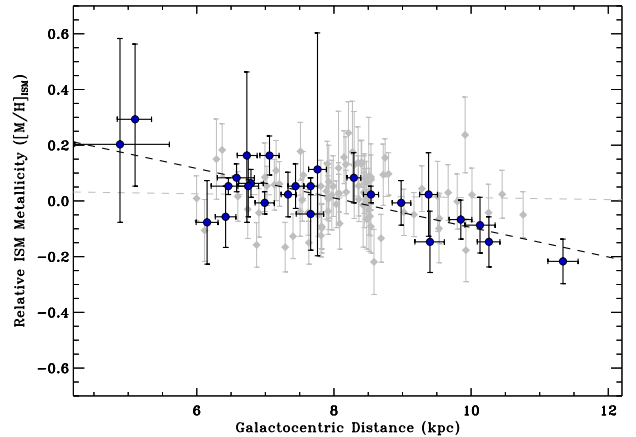


Figure 14. Relative metallicities of H II regions and neutral clouds in the Galactic disk plotted as a function of Galactocentric distance (R_G). The blue symbols represent the oxygen abundances derived for a sample of H II regions located within 4 kpc of the Sun (Arellano-Córdova et al. 2020, 2021), normalized by the oxygen abundance at the solar circle (i.e., at $R_G = 8.2$ kpc). The diagonal dashed line indicates the radial abundance gradient that pertains to the H II regions. The light gray points represent the relative ISM metallicities derived in this work for sight lines probing neutral gas in the solar neighborhood (out to 4 kpc). The light gray dashed line indicates a linear fit to these data points.

sity should be attributed to those components showing weaker depletions. However, a simpler (and we would argue more likely) explanation is that the metallicities in the various line-of-sight components are roughly equivalent whereas the physical conditions (and hence the depletion strengths) are the quantities that vary from one gas region to the next.

5.2. Metallicity Variations in the Galactic Disk

Having completed our examination of the distribution of metallicities in the neutral ISM, it is instructive to compare our results to those obtained from other tracers of metallicity in the Galactic disk. Recently, Esteban et al. (2022) presented a comparison of the metallicity distributions derived from studies of H II regions, neutral clouds, B stars, Cepheids, and young clusters. The dispersions in the metallicities derived from H II regions (Arellano-Córdova et al. 2020, 2021), B stars (Nieva & Przybilla 2012), Cepheids (Luck 2018), and young clusters (Donor et al. 2020) within 3 kpc of the Sun are all similar to one another and are all $\lesssim 0.10$ dex. For neutral clouds, Esteban et al. (2022) cite the results of De Cia et al. (2021) finding that only in this case is the dispersion in metallicity much larger (~ 0.28 dex). If our more extensive survey of neutral cloud metallicities were considered instead, the dispersion would be ~ 0.10 dex (Section 4.3), similar to the

⁷ These authors have softened their conclusions somewhat in an addendum to their original article (De Cia et al. 2022).

values obtained from other constituents of the Galactic disk.

In Figure 14, we plot the (relative) metallicities derived for a sample of H II regions located within 4 kpc of the Sun (Arellano-Córdova et al. 2020, 2021) against the Galactocentric distances of those H II regions (Méndez-Delgado et al. 2022). The plotted values are the total oxygen abundances of the ionized nebulae normalized by the oxygen abundance at the solar circle (i.e., at $R_G = 8.2$ kpc). The diagonal dashed line in the figure, which was used to determine this offset, indicates the radial abundance gradient that pertains to the H II regions.⁸ Also shown in Figure 14 are the relative ISM metallicities derived in this work for sight lines probing neutral clouds in the solar neighborhood (out to 4 kpc). (For this figure, we adopt the values of $[M/H]_{\text{ISM}}$ obtained from the fits that exclude the refractory elements.) There is no evidence of an abundance gradient from our determinations of $[M/H]_{\text{ISM}}$, as shown by the light gray dashed line in the figure. However, the overall dispersion in the relative metallicities of the neutral clouds is similar to that of the H II regions within 4 kpc of the Sun.

An important caveat regarding the comparison of relative metallicities shown in Figure 14 is that, in general, the distances to the interstellar clouds seen in absorption toward background stars are not the same as the distances to the stars themselves. In contrast, the H II regions are actually located at the Galactocentric distances plotted in the figure (or presumably so within the uncertainties). Typically, the dominant absorption components toward the stars in our survey are found near $v_{\text{LSR}} = 0$ km s⁻¹. While many of the more distant stars exhibit multiple absorption complexes, corresponding to gas in different spiral arms (such as the Sagittarius-Carina spiral arm or the Perseus spiral arm), the “local arm” component near $v_{\text{LSR}} = 0$ km s⁻¹ is usually the strongest. This suggests that much of the interstellar material along the various sight lines in our survey is (kinematically) close to the Sun, regardless of the distance to the background star. This may then explain why no abundance gradient is apparent in the metallicity data presented here for neutral clouds.

⁸ We plot *relative* metallicities for the H II regions in Figure 14 so that the values can be more directly compared to our results for neutral clouds. Also, in this way, we avoid the so-called “abundance discrepancy problem”, where the abundances obtained from collisionally excited lines in ionized nebulae are systematically lower than the abundances derived from recombination lines. The abundance discrepancy for O may explain why the H II region O abundances are offset from the solar value by ~ 0.2 dex (e.g., see Arellano-Córdova et al. 2020; Esteban et al. 2022).

6. CONCLUSIONS

In this investigation, we have presented an analysis of relative ISM metallicities for a sample of 84 sight lines probing diffuse neutral gas in the solar neighborhood out to a maximum heliocentric distance of 4 kpc. The methodology we employ was first proposed by Jenkins (2009) as a means to study the dust depletions and metallicities in high redshift absorption systems. The essence of this approach is to compare the pattern of relative abundances seen for a variety of elements in a given direction to the expected trends due to the depletion of atoms from the gas-phase onto interstellar dust grains. This comparison then yields the overall strength of depletion along the line of sight and whether the abundances collectively are higher or lower than the average interstellar abundances. While this method cannot provide the metallicity of the ISM with respect to some adopted cosmic abundance standard, it can yield useful information on the spread in the metallicities that pertain to neutral gas in the solar neighborhood.

To accomplish our objective of determining the metallicity distribution for a representative sample of sight lines probing the local Galactic ISM, we compiled a database of high-quality column density measurements reported in the literature for 22 elements that had previously been analyzed in accordance with the methodology devised by Jenkins (2009). The vast majority of column density measurements used in the metallicity analysis were derived from observations acquired with STIS or GHRS. However, for some elements (i.e., N, Cl, and Fe), many of the column densities adopted here were obtained from lower resolution FUSE spectra. The column density measurements adopted for Ti were derived using a variety of ground-based instruments, such as VLT/UVES. We supplemented the literature survey with new column density determinations for certain key elements (e.g., Ti and Ni) and for several interesting and/or important sight lines (see Section 3.2).

In order to properly constrain the least-squares linear fits that yielded values of $[M/H]_{\text{ISM}}$, we required that each line of sight have column density measurements for at least eight different elements. An initial inspection of the linear fits revealed a persistent nonlinearity in the trends of y versus x that would cause the slope and y -intercept of the fit to be underestimated. We attribute this nonlinearity to a situation where a line of sight passes through multiple distinct gas regions with different depletion properties. A simple solution was to exclude the most refractory elements from the linear fits so as to obtain the depletion strength and metallicity for the bulk of the material along the line of sight.

Regardless of the set of relative ISM metallicities that is considered (Table 5), the results of our analysis are clear. The dispersion in the metallicities that pertain to neutral gas in the solar neighborhood is small (~ 0.10 dex) and only slightly larger than the typical measurement uncertainties. These results stand in sharp contrast to those presented by De Cia et al. (2021), who reported metallicities as low as -0.76 dex, a mean metallicity of -0.26 dex, and a dispersion of 0.28 dex for a sample of 25 sight lines. We find no evidence for the existence of very low metallicity ($[M/H] \lesssim -0.3$ dex) gas along any of the 84 sight lines in our survey. There are eight sight lines in common between our investigation and that of De Cia et al. (2021). In each case, our value for the relative ISM metallicity is substantially larger (by 0.2 to 0.8 dex) compared to the value given in De Cia et al. (2021). The reason for these discrepancies is that there are serious flaws in the analysis undertaken by De Cia et al. (2021). The Zn II column densities reported by De Cia et al. (2021) are likely underestimated since they are based on integrated column densities derived using relatively strong absorption features recorded at moderate resolution. A more serious concern is that the metallicity determinations in De Cia et al. (2021) are based on linear fits that include only the most refractory elements. Volatile elements, which are better tracers of metallicity in the diffuse ISM, are excluded from their analysis even though they yield conflicting results.

The dispersion in the metallicities that we obtain for sight lines probing the neutral ISM is similar to the values reported for other tracers of metallicity in the Galactic disk. The metallicity distributions for neutral clouds, H II regions, B stars, Cepheids, and young clusters in the solar neighborhood all have dispersions of ~ 0.10 dex or lower. Together, these results provide strong observational support for a well-mixed, chemically homogeneous ISM in the vicinity of the Sun.

We note the passing of our scientific colleague, Prof. Blair Savage, on July 19, 2022 in Madison, WI. Blair was a major figure in UV space astronomy who, with his students, postdocs, and colleagues, made seminal contributions to studies of gas and dust in the interstellar and intergalactic medium. We thank Dan Welty for providing useful comments on an early draft of this paper. We also thank the anonymous referee for helpful suggestions that improved our analysis. This research has made use of the SIMBAD database operated at CDS, Strasbourg, France. Observations were obtained from the ESO Science Archive Facility and the MAST data archive at the Space Telescope Science Institute. STScI is operated by the Association of Universities for Research in Astronomy, Inc., under NASA contract NAS5-26555.

Facilities: HST(STIS, GHRS), FUSE, VLT(UVES)

Software: ISMOD (Sheffer et al. 2008), STSDAS

APPENDIX

A. COMPILATION OF COLUMN DENSITY MEASUREMENTS FOR METAL IONS

A complete compilation of the column densities used in the metallicity analysis (described in Section 4) for elements other than hydrogen is provided in Table 6. For each entry in the table, we provide the reference for the column density measurement (see codes listed in Table 3), the instrument that recorded the spectrum, and the method used in the analysis. The instrument codes include FUSE, GHRS, OPT, STIS, and UVES (where OPT refers to any ground-based optical telescope other than VLT/UVES). The method codes include AOD, COG, FIT, LDW, and WLL (which are explained in a footnote to Table 6). Note that in some cases a combination of instruments and/or methods were used. All column densities listed in Table 6 have been adjusted so as to be consistent with the set of f -values provided in Table 2.

In Table 7, we provide additional details regarding the column density measurements newly-derived in this investigation (see Section 3.2). In particular, we provide the equivalent widths (W_λ) and column densities of the individual transitions analyzed in each direction. All of the results listed in Table 7 (except those for Ti II) were derived from high-resolution (E140H or E230H) STIS spectra using either the AOD or profile fitting method. The Ti II column densities were extracted from archival VLT/UVES spectra using the AOD approach. In cases where multiple transitions from the same species were analyzed, final column densities were obtained by taking the weighted mean of the individual results. The final column densities in these cases are provided in Table 6.

REFERENCES

- Alkhatat, R. B., Irving, R. E., Federman, S. R., Ellis, D. G., & Cheng, S. 2019, ApJ, 887, 14
- André, M. K., Oliveira, C. M., Howk, J. C., et al. 2003, ApJ, 591, 1000

Table 6. Column Densities Used in the Metallicity Analysis

Star	Species	$\log N$	Reference ^a	Instrument	Method ^b
HD 1383	B II	11.92 ± 0.07	RFSL11	STIS	FIT
	O I	18.15 ± 0.02	RFL18	STIS	FIT
	Mg II	16.36 ± 0.09	CLMS06	STIS	FIT
	P II	14.56 ± 0.04	RBFS23	STIS	FIT
	Mn II	13.76 ± 0.06	CLMS06	STIS	FIT
	Ni II	14.00 ± 0.03	CLMS06	STIS	FIT
	Cu II	12.77 ± 0.05	RFSL11	STIS	FIT
	Ga II	12.07 ± 0.05	RFSL11	STIS	FIT
	Ge II	12.74 ± 0.02	RFL18	STIS	FIT
	Kr I	12.52 ± 0.08	RFL18	STIS	FIT
HD 12323	Sn II	11.88 ± 0.12	RFL18	STIS	FIT
	O I	18.02 ± 0.06	CLMS04	STIS	FIT
	Mg II	16.04 ± 0.05	CLMS06	STIS	FIT
	P II	14.45 ± 0.04	RBFS23	STIS	FIT
	Cl I+Cl II	14.36 ± 0.05	RBFS23	FUSE+STIS	FIT
	Mn II	13.69 ± 0.08	CLMS06	STIS	FIT
	Fe II	15.13 ± 0.07	JS07	FUSE	COG
	Ni II	14.02 ± 0.03	CLMS06	STIS	FIT
	Cu II	12.53 ± 0.05	CLMS06	STIS	FIT
	Ge II	12.30 ± 0.06	CLMS06	STIS	FIT

NOTE—This table is available in its entirety in machine-readable form.

^aReference codes used in this table are explained in Table 3.

^bMethod used in the column density determination. The codes listed have the following meaning: AOD: apparent optical depth integration; COG: curve of growth analysis; FIT: Voigt profile fitting analysis; LDW: analysis of Lorentzian damping wings; WLL: weak line limit calculation.

Arellano-Córdova, K. Z., Esteban, C., García-Rojas, J., & Méndez-Delgado, J. E. 2020, *MNRAS*, 496, 1051
 Arellano-Córdova, K. Z., Esteban, C., García-Rojas, J., & Méndez-Delgado, J. E. 2021, *MNRAS*, 502, 225
 Asplund, M., Amarsi, A. M., & Grevesse, N. 2021, *A&A*, 653, A141
 Bailer-Jones, C. A. L., Rybizki, J., Foesneau, M., Demleitner, M., & Andrae, R. 2021, *AJ*, 161, 147
 Boissé, P., & Bergeron, J. 2019, *A&A*, 622, A140
 Brown, M. S., Alkhayat, R. B., Irving, R. E., et al. 2018, *ApJ*, 868, 42
 Brown, M. S., Federman, S. R., Irving, R. E., Cheng, S., & Curtis, L. J. 2009, *ApJ*, 702, 880
 Cardelli, J. A. 1994, *Sci*, 265, 209
 Cardelli, J. A., Federman, S. R., Lambert, D. L., & Theodosiou, C. E. 1993b, *ApJL*, 416, L41
 Cardelli, J. A., Mathis, J. S., Ebbets, D. C., & Savage, B. D. 1993a, *ApJL*, 402, L17

Cardelli, J. A., & Meyer, D. M. 1997, *ApJL*, 477, L57
 Cardelli, J. A., Meyer, D. M., Jura, M., & Savage, B. D. 1996, *ApJ*, 467, 334
 Cardelli, J. A., Savage, B. D., Bruhweiler, F. C., et al. 1991a, *ApJL*, 377, L57
 Cardelli, J. A., Savage, B. D., & Ebbets, D. C. 1991b, *ApJL*, 383, L23
 Cardelli, J. A., Sofia, U. J., Savage, B. D., Keenan, F. P., & Dufton, P. L. 1994, *ApJL*, 420, L29
 Cartledge, S. I. B., Lauroesch, J. T., Meyer, D. M., & Sofia, U. J. 2004, *ApJ*, 613, 1037
 Cartledge, S. I. B., Lauroesch, J. T., Meyer, D. M., & Sofia, U. J. 2006, *ApJ*, 641, 327
 Cartledge, S. I. B., Lauroesch, J. T., Meyer, D. M., Sofia, U. J., & Clayton, G. C. 2008, *ApJ*, 687, 1043
 Cartledge, S. I. B., Meyer, D. M., & Lauroesch, J. T. 2003, *ApJ*, 597, 408

Table 7. New Column Density Determinations

Star	Transition	W_λ (mÅ)	$\log N$	Method ^a
HD 14434	Fe II λ 2249	155.4 ± 3.1	15.39 ± 0.01	FIT
	Fe II λ 2260	193.9 ± 3.1	15.39 ± 0.01	FIT
HD 15137	Cr II λ 2056	99.5 ± 3.4	13.54 ± 0.02	FIT
	Cr II λ 2062	78.5 ± 3.3	13.55 ± 0.02	FIT
	Cr II λ 2066	57.8 ± 3.0	13.55 ± 0.02	FIT
	Ni II λ 1317	65.4 ± 1.8	14.01 ± 0.04	AOD
	Ni II λ 1454	39.1 ± 2.7	14.04 ± 0.12	AOD
	Ni II λ 1709	71.0 ± 6.1	14.03 ± 0.05	AOD
	Ni II λ 1741	93.6 ± 4.4	14.04 ± 0.04	AOD
	Ni II λ 1751	69.5 ± 4.8	14.04 ± 0.05	AOD
HD 23180	Ti II λ 3383	6.6 ± 0.5	11.26 ± 0.04	AOD
	Ni II λ 1317	9.9 ± 0.4	13.11 ± 0.02	FIT
	Ni II λ 1370	12.1 ± 0.3	13.15 ± 0.02	FIT
HD 24190	Mg II λ 1239	28.0 ± 0.4	15.67 ± 0.02	FIT
	Mg II λ 1240	18.6 ± 0.3	15.68 ± 0.02	FIT
	Mn II λ 1197	27.6 ± 0.7	13.34 ± 0.03	FIT
	Mn II λ 1201	20.4 ± 0.8	13.39 ± 0.02	FIT
	Ni II λ 1317	12.3 ± 0.3	13.21 ± 0.01	FIT
	Ni II λ 1370	14.0 ± 1.1	13.23 ± 0.03	FIT

NOTE—This table is available in its entirety in machine-readable form.

^aMethod codes used here have the same meaning as in Table 6.

- Cartledge, S. I. B., Meyer, D. M., Lauroesch, J. T., & Sofia, U. J. 2001, *ApJ*, 562, 394
- Cashman, F. H., Kulkarni, V. P., Kisielius, R., Ferland, G. J., & Bogdanovich, P. 2017, *ApJS*, 230, 8
- Chiappini, C., Matteucci, F., & Gratton, R. 1997, *ApJ*, 477, 765
- de Avillez, M. A., & Mac Low, M.-M. 2002, *ApJ*, 581, 1047
- De Cia, A., Jenkins, E. B., Fox, A. J., et al. 2021, *Nature*, 597, 206
- De Cia, A., Jenkins, E. B., Fox, A. J., et al. 2022, *Nature*, 605, E8
- Diplas, A., & Savage, B. D. 1994, *ApJS*, 93, 211
- Donor, J., Frinchaboy, P. M., Cunha, K., et al. 2020, *AJ*, 159, 199
- Dwek, E., & Scalo, J. M. 1980, *ApJ*, 239, 193
- Edmunds, M. G. 1975, *Ap&SS*, 32, 483
- Esteban, C., Méndez-Delgado, J. E., García-Rojas, J., & Arellano-Córdova, K. Z. 2022, *ApJ*, 931, 92
- Federman, S. R., Brown, M., Torok, S., et al. 2007, *ApJ*, 660, 919
- Federman, S. R., Lambert, D. L., Sheffer, Y., et al. 2003, *ApJ*, 591, 986
- François, P., Matteucci, F., Cayrel, R., et al. 2004, *A&A*, 421, 613
- Heidarian, N., Irving, R. E., Federman, S. R., et al. 2017, *JPhB*, 50, 155007
- Heidarian, N., Irving, R. E., Ritchey, A. M., et al. 2015, *ApJ*, 808, 112
- Hobbs, L. M., Welty, D. E., Morton, D. C., Spitzer, L., & York, D. G. 1993, *ApJ*, 411, 750
- Jenkins, E. B. 1996, *ApJ*, 471, 292
- Jenkins, E. B. 2009, *ApJ*, 700, 1299
- Jenkins, E. 2013, in *Proc. of The Life Cycle of Dust in the Universe: Observations, Theory, and Laboratory Experiments*, ed. A. Andersen et al. (Trieste: SISSA), 5
- Jenkins, E. B. 2019, *ApJ*, 872, 55
- Jenkins, E. B., Savage, B. D., & Spitzer, L. 1986, *ApJ*, 301, 355
- Jenkins, E. B., & Tripp, T. M. 2006, *ApJ*, 637, 548
- Jensen, A. G., Rachford, B. L., & Snow, T. P. 2007, *ApJ*, 654, 955
- Jensen, A. G., & Snow, T. P. 2007, *ApJ*, 669, 378
- Jones, A. P., Tielens, A. G. G. M., Hollenbach, D. J., & McKee, C. F. 1994, *ApJ*, 433, 797

- Jura, M., & York, D. G. 1978, *ApJ*, 219, 861
- Kisielius, R., Kulkarni, V. P., Ferland, G. J., et al. 2015, *ApJ*, 804, 76
- Knauth, D. C., Andersson, B-G, McCandliss, S. R., & Moos, H. W. 2003, *ApJL*, 596, L51
- Knauth, D. C., Meyer, D. M., & Lauroesch, J. T. 2006, *ApJL*, 647, L115
- Lambert, D. L., Sheffer, Y., Federman, S. R., et al. 1998, *ApJ*, 494, 614
- Lodders, K. 2003, *ApJ*, 591, 1220
- Luck, R. E. 2018, *AJ*, 156, 171
- Lundberg, H., Hartman, H., Engstrom, L., et al. 2016, *MNRAS*, 460, 356
- Méndez-Delgado, J. E., Amayo, A., Arellano-Córdova, K. Z., et al. 2022, *MNRAS*, 510, 4436
- Meyer, D. M., Cardelli, J. A., & Sofia, U. J. 1997, *ApJL*, 490, L103
- Meyer, D. M., Jura, M., & Cardelli, J. A. 1998, *ApJ*, 493, 222
- Miller, A., Lauroesch, J. T., Sofia, U. J., Cartledge, S. I. B., & Meyer, D. M. 2007, *ApJ*, 659, 441
- Morton, D. C. 2000, *ApJS*, 130, 403
- Morton, D. C. 2003, *ApJS*, 149, 205
- Nieva, M.-F., & Przybilla, N. 2012, *A&A*, 539, A143
- Oliver, P., & Hibbert, A. 2013, *ADNDT*, 99, 459
- Petit, A. C., Krumholz, M. R., Goldbaum, N. J., & Forbes, J. C. 2015, *MNRAS*, 449, 2588
- Press, W. H., Teukolsky, S. A., Vetterling, W. T., & Flannery, B. P. 2007, *Numerical Recipes, The Art of Scientific Computing* (3rd ed.; Cambridge: Cambridge Univ. Press)
- Rachford, B. L., Snow, T. P., Tumlinson, J. D., et al. 2009, *ApJS*, 180, 125
- Rachford, B. L., Snow, T. P., Tumlinson, J., et al. 2002, *ApJ*, 577, 221
- Ritchey, A. M., Federman, S. R., & Lambert, D. L. 2018, *ApJS*, 236, 36
- Ritchey, A. M., Federman, S. R., Sheffer, Y., & Lambert, D. L. 2011, *ApJ*, 728, 70
- Ritchey, A. M., Brown, J. M., Federman, S. R., & Sonnentrucker, P. 2023, *ApJ*, in press [arXiv:2301.09727]
- Roth, K. C., & Blades, J. C. 1995, *ApJL*, 445, L95
- Roy, J.-R., & Kunth, D. 1995, *A&A*, 294, 432
- Savage, B. D., Cardelli, J. A., & Sofia, U. J. 1992, *ApJ*, 401, 706
- Savage, B. D., & Sembach, K. R. 1991, *ApJ*, 379, 245
- Savage, B. D., & Sembach, K. R. 1996, *ARA&A*, 34, 279
- Schechtman, R. M., Federman, S. R., Brown, M., et al. 2005, *ApJ*, 621, 1159
- Seab, C. G., & Shull, J. M. 1983, *ApJ*, 275, 652
- Sembach, K. R., & Savage, B. D. 1996, *ApJ*, 457, 211
- Sheffer, Y., Rogers, M., Federman, S. R., et al. 2008, *ApJ*, 687, 1075
- Shull, J. M., York, D. G., & Hobbs, L. M. 1977, *ApJL*, 211, L139
- Slavin, J. D., Dwek, E., & Jones, A. P. 2015, *ApJ*, 803, 7
- Snow, T. P., Rachford, B. L., & Figoski, L. 2002, *ApJ*, 573, 662
- Snow, T. P., Rachford, B. L., Tumlinson, J., et al. 2000, *ApJL*, 538, L65
- Sofia, U. J., Cardelli, J. A., Guerin, K. P., & Meyer, D. M. 1997, *ApJL*, 482, L105
- Sofia, U. J., Cardelli, J. A., & Savage, B. D. 1994, *ApJ*, 430, 650
- Sofia, U. J., Lauroesch, J. T., Meyer, D. M., & Cartledge, S. I. B. 2004, *ApJ*, 605, 272
- Sofia, U. J., Meyer, D. M., & Cardelli, J. A. 1999, *ApJL*, 522, L137
- Sonnentrucker, P., Friedman, S. D., Welty, D. E., York, D. G., & Snow, T. P. 2002, *ApJ*, 576, 241
- Sonnentrucker, P., Friedman, S. D., Welty, D. E., York, D. G., & Snow, T. P. 2003, *ApJ*, 596, 350
- Sonnentrucker, P., Welty, D. E., Thorburn, J. A., & York, D. G. 2007, *ApJS*, 168, 58
- Spitzer, L. 1985, *ApJL*, 290, L21
- Timmes, F. X., Woosley, S. E., & Weaver, T. A. 1995, *ApJS*, 98, 617
- Toner, A., & Hibbert, A. 2005, *MNRAS*, 361, 673
- Welty, D. E. 2007, *ApJ*, 668, 1012
- Welty, D. E., & Crowther, P. A. 2010, *MNRAS*, 404, 1321
- Welty, D. E., Hobbs, L. M., Lauroesch, J. T., et al. 1999, *ApJS*, 124, 465
- Welty, D. E., Hobbs, L. M., Lauroesch, J. T., Morton, D. C., & York, D. G. 1995, *ApJL*, 449, L135
- Welty, D. E., Sonnentrucker, P., Snow, T. P., & York, D. G. 2020, *ApJ*, 897, 36
- Yang, C.-C., & Krumholz, M. 2012, *ApJ*, 758, 48